White Rose Research Online

eprints@whiterose.ac.uk
https://eprints.whiterose.ac.uk
Universities of Leeds, Sheffield and York

Deposited via The University of Sheffield.

White Rose Research Online URL for this paper:
https://eprints.whiterose.ac.uk/id/eprint/247208/

Version: Published Version

Article:
Mallaghan, N., de Mooij, E.J.W., Watson, C.A. et al. (2026) NGTS clusters survey – VII. An enigmatic short-period circumsecondary disc candidate in Orion. Monthly Notices of the Royal Astronomical Society, 552 (3). stag1802. ISSN: 0035-8711

https://doi.org/10.1093/mnras/stag1802

Reuse
This article is distributed under the terms of the Creative Commons Attribution (CC BY) licence. This licence allows you to distribute, remix, tweak, and build upon the work, even commercially, as long as you credit the authors for the original work. More information and the full terms of the licence here: https://creativecommons.org/licenses/

Takedown
If you consider content in White Rose Research Online to be in breach of UK law, please notify us by emailing eprints@whiterose.ac.uk including the URL of the record and the reason for the withdrawal request.

UNIVERSITY OF LEEDS
University of Sheffield
UNIVERSITY of York

Monthly Notices of the ROYAL ASTRONOMICAL SOCIETY

MNRAS **552,** 1–18 (2026)
Advance Access publication 2026 September 24

https://doi.org/10.1093/mnras/stag1802

NGTS clusters survey – VII. An enigmatic short-period circumsecondary disc candidate in Orion

Niamh Mallaghan [1★] Ernst J. W. de Mooij [1] Christopher A. Watson [1] Edward Gillen [2] Matthew Kenworthy [3] Louise D. Nielsen [4] David R. Anderson [5] Matthew P. Battley [2] Edward M. Bryant [6,7] Matthew R. Burleigh [8] Benjamin M. J. Cadell [1] Sarah L. Casewell [8] Alexander Chaushev,[9] V. S. Dhillon [10,11] Elsa Ducrot [12,13] Jorge Fernández Fernández [6,7] Samuel Gill [6,7] Michaël Gillon [14] Michael R. Goad [8] Faith Hawthorn [6,7,15] Katlyn L. Hobbs [1] James McCormac [6,7] Maximiliano Moyano,[5] Catriona A. Murray [16] Toby Rodel [1] Suman Saha [17,18] Ramotholo R. Sefako,[19] John Southworth [20] Mathilde Timmermans [21] Amaury H. M. J. Triaud [21] Jose Vines [5] Richard G. West [6,7] Peter J. Wheatley [6,7] and Tafadzwa Zivave [6,7]

Affiliations are listed at the end of the paper

Accepted 2026 September 21. Received 2026 September 21; in original form 2026 June 12

ABSTRACT

Young stellar systems provide key insights into the processes governing star/planet formation, often exhibiting complex and evolving photometric variability. In this paper, we present an analysis of the object around NOI 105872, observed by the Next Generation Transit Survey (NGTS) to eclipse a young (4.1 ± 0.4 Myr) M-type star in the Orion Nebula Cluster. The system displays deep, asymmetric eclipses with a period of ~ 0.69 d, alongside variability in morphology. We combine photometric observations spanning approximately a decade from multiple ground- and space-based facilities to investigate the nature of this system. We explore a range of physical scenarios to reproduce the eclipse profiles and their evolution. After analysis, our preferred explanation is a circumsecondary disc surrounding a companion in orbit around the M-type primary. We adopt a six-parameter disc model and fit the eclipse profiles independently to each data set. The best-fitting solution yields a disc radius of ~ 0.005 au or $0.98\,R_*$, with broadly consistent orientations across epochs, but with variations that may be attributed to disc precession or intrinsic stellar variability. Constraints from the Hill radius imply a companion mass consistent with a very low-mass stellar companion. These results establish NOI 105872 as a candidate for a circumsecondary disc system in a young stellar environment. Continued photometric monitoring and spectroscopic follow-up will be essential to confirm this interpretation. If confirmed, systems such as NOI 105872 provide valuable benchmarks for understanding disc dynamics, companion formation, and the origin of complex eclipse phenomena in young stars.

Key words: exoplanets – planets and satellites: general.

1 INTRODUCTION

Young stellar clusters provide some of the most powerful laboratories for understanding the processes that govern star and planet formation. In these environments, populations of coeval stars (stars that formed at the same time and from the same molecular cloud) with similar initial chemical compositions, but a range of masses and evolutionary stages, allow us to isolate the physical mechanisms that shape stellar evolution (C. J. Lada & E. A. Lada 2003; S. F. Portegies Zwart, S. L. W. McMillan & M. Gieles 2010). In particular, open clusters and star-forming regions offer a statistically rich sample for investigating early stellar variability, circumstellar disc evolution, and the onset of planet formation.

Wide-field time-domain surveys of clusters have significantly advanced this field by enabling high-precision, long-baseline photometric monitoring of young stellar populations. In particular, surveys such as the Next Generation Transit Survey (NGTS; P. J. Wheatley et al. 2018) have demonstrated the value of cluster observations in identifying and characterizing variable young stars and substellar companions (E. Gillen et al. 2020; J. A. G. Jackman et al. 2020; G. D. Smith et al. 2021; T. Moulton et al. 2023; G. D. Smith et al. 2023). These data sets have revealed complex and often unexpected light curve morphologies that are closely linked to the presence of circumstellar material and dynamical interactions in young systems.

★ E-mail: nmallaghan01@qub.ac.uk

© The Author(s) 2026.
Published by Oxford University Press on behalf of Royal Astronomical Society. This is an Open Access article distributed under the terms of the Creative Commons Attribution License (https://creativecommons.org/licenses/by/4.0/), which permits unrestricted reuse, distribution, and reproduction in any medium, provided the original work is properly cited.

Downloaded from academic.oup.com/mnras/article/552/3/stag1802/8834030 by University of Sheffield user on 29 October 2026

One of the most intriguing outcomes of such surveys is the identification of unusual eclipse and dimming behaviour in young stellar objects. A prominent class of these are 'dipper' stars, which exhibit quasi-periodic flux dips thought to arise from occultations by circumstellar disc material located at or near the inner disc edge (M. Ansdell et al. 2016; A. M. Cody & L. A. Hillenbrand 2018). These systems provide direct insight into disc structure, inclination effects, and dust evolution in planet-forming environments.

In addition to dipper stars, a broader range of complex periodic variables have been identified in young clusters, exhibiting non-sinusoidal, evolving, or multicomponent variability (A. M. Cody et al. 2014; A. McQuillan, T. Mazeh & S. Aigrain 2014; L. M. Rebull et al. 2014). These behaviours are often attributed to a combination of starspot modulation, accretion variability, warped inner discs, and occulting material in asymmetric configurations. Such systems highlight the dynamic and often unstable nature of early stellar environments.

Even more extreme examples of unusual eclipse signatures have been observed in young and pre-main sequence systems where circumstellar or circumbinary dust produces large-amplitude, often highly structured photometric variability. The best-known example is J1407b, which exhibited a deep, long-duration and complex eclipse interpreted as the transit of an extensive ring system or circumplanetary material (E. E. Mamajek et al. 2012). Similar dust-related eclipses have been reported in V928 Tau, although no clear periodicity has yet been established (D. M. Dam et al. 2020). Other pre-main sequence variables, including V718 Per and CHS 7797, display approximately sinusoidal brightness variations attributed to obscuration by circumstellar material, despite having markedly different periods of 4.7 yr and 17.8 d, respectively (V. Grinin et al. 2008; M. V. Rodríguez-Ledesma et al. 2013).

Several of these objects are often compared to KH 15D, the prototype of a class of eclipsing pre-main sequence binaries in which a misaligned circumbinary disc periodically obscures one or both stellar components (K. E. Kearns & W. Herbst 1998). Photometric and spectroscopic studies have demonstrated that the disc in KH 15D is significantly tilted relative to its highly eccentric central binary, producing the system's distinctive long-duration eclipses (e.g. E. I. Chiang & R. A. Murray-Clay 2004; J. N. Winn et al. 2004). More recently, searches for analogous systems have identified additional candidates, including ZTF J202055.22+381323.1 and ZTF J071445.39−090152.1, whose variability is likewise consistent with obscuration by circumbinary material (W. Zhu et al. 2022). Long-term monitoring has shown that the amplitudes of these systems can evolve substantially with time, reflecting changes in viewing geometry and disc structure. Collectively, these objects demonstrate the wide range of eclipse morphologies produced by circumstellar and circumbinary dust and highlight the importance of time-domain surveys in identifying new examples of disc-related eclipsing systems.

Together, these classes of objects demonstrate that variability in young stellar clusters can uncover a rich diagnostic of circumstellar structure, disc evolution, and early planetary system architecture. In this work, we present an analysis of the enigmatic NOI 105872, situated within this broader context of young stellar variability and eclipse phenomenology. First identified in the Orion Nebula Cluster (ONC) by NGTS in August 2017, observations revealed a persistent periodic and asymmetric eclipsing signal.

In this work, we combine photometric data from multiple telescopes to model the light curves of NOI 105872 in a range of different scenarios, including orbital dynamics (highly eccentric orbit), stellar effects (stellar activity, 'dipper' stars, gravity darkening, complex periodic variables), and exotic companions (evaporating planet, tilted disc system). One of the most plausible hypotheses for explaining its unusual light curves is the presence of a tilted circumsecondary disc around a companion object. We investigate the geometry and properties of the hypothesized disc. By fitting parametric disc models to the observed eclipses, we aim to constrain its size, orientation, and variability, and to explore the implications for disc evolution and planet formation around low-mass stars.

2 PHOTOMETRIC OBSERVATIONS

NOI 105872 was initially observed by NGTS in 2017 as part of a survey field and is identified in *GAIA* by Gaia DR3 3 023 459 583 984 210 304 with a mean magnitude of G = 15.5 mag. It is also identified in the 2MASS catalogue by 2MASS J05395645−0420140, with a *K*-band magnitude of 11.9 mag, and in *TESS* by TIC 11356619. There were subsequently a number of eclipses observed both during other telescope surveys and as targeted follow-up. A summary of these photometric observations is presented in Table 1.

2.1 NGTS

The Next Generation Transit Survey (NGTS) is a collection of 12 robotic ground-based telescopes situated at the ESO Paranal Observatory (P. J. Wheatley et al. 2018). Each telescope is 20 cm in diameter, with a wide field of view (2.8 × 2.8 deg) and uses a custom filter that covers wavelengths from 520 to 890 nm. Specifically, this bandpass is particularly sensitive to early M type stars, which is beneficial in the case of NOI 105872. Observations by NGTS were reduced by a custom-built modular pipeline as described in P. J. Wheatley et al. (2018).

NOI 105872 was first observed and discovered during a survey of Orion in 2017. We detected multiple eclipses and it was flagged as an NGTS Object of Interest (NOI). Objects in the NGTS data are searched through for transits/eclipses and rotation signals. This object (with both clear eclipses and rotation) was detected. Between 2017 August 16 and 2018 March 17 it was observed for a total of 213 nights, the longest period of continuous observation for this object to date, and Fig. 1 shows the phase-folded light curve. Initially, NOI 105872 was not flagged as anything peculiar; however, as more data from other telescopes was collected, this object became more difficult to constrain. Between 2021 December 08 and 2022 February 24, the object was observed for a further 78 nights. The eclipse depth changes from 6 per cent to 10 per cent, and the eclipse duration in the second data set appears to be lengthened compared to the first, as seen in Epoch 1 and 5 of Fig. 2(b).

2.2 *TESS*

The *Transiting Exoplanet Survey Satellite* (*TESS*) is a NASA space telescope launched in 2018 to complete an all-sky survey of nearby bright stars with the aim of finding transiting exoplanets (G. R. Ricker et al. 2015). The spacecraft houses four wide-field cameras with a bandpass of 600–1000 nm with observations being split into sectors, periods of around 27 d of nearly continuous

Downloaded from academic.oup.com/mnras/article/552/3/stag1802/8834030 by University of Sheffield user on 29 October 2026

Table 1. Summary of photometric observations of NOI 105872. Eclipse depth values quoted are approximate values for comparison between epochs.

Telescope	Obs dates	Wavelengths (nm)	Exp time (s)	$N_{\rm points}$	Eclipse depth
NGTS	2017 Aug 16–2018 Mar 17	520–890	10	162 139	6 per cent-8 per cent
TESS Sector 6	2018 Dec 15–2019 Jan 06	600–1000	1800	987	13 per cent
SAAO	2020 Jan 03	700–900	60	350	7 per cent
SPECULOOS	2020 Jan 28–2020 Jan 29	750–1000	50	335	7.5 per cent
ULTRASPEC	2020 Feb 02	400–540	15	1239	11.5 per cent
TESS Sector 32	2020 Nov 20–2020 Dec 16	600–1000	600	3459	8.5 per cent
NGTS	2021 Dec 09–2022 May 22	520–890	10	34 098	9–10 per cent
ATLAS	2015–2025	560–820	30	2279	5–10 per cent

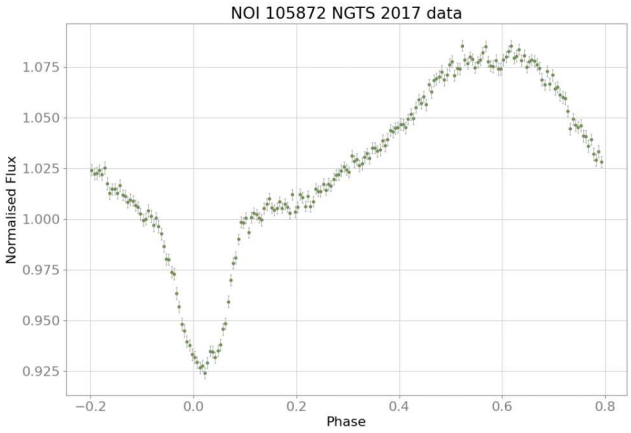


Figure 1. NGTS phase-folded light curve from the original observed data in 2017–18, using a period of 0.691 d. The data are binned into 200 data points.

observation, depending on which part of the sky is being surveyed at that time.

For our analysis of NOI 105872, we generated custom light curves directly from the *TESS* Science Processing Operations Centre (SPOC; J. M. Jenkins et al. 2016) Full-Frame images. This was done as the SPOC and Quick Look Pipeline (QLP; C. X. Huang et al. 2020) light curves for this star were not always available when we needed them for our analysis. It also allowed us to tailor the photometric aperture and background pixel mask to suit NOI 105872 in each *TESS* sector. We used the LIGHTKURVE package (Lightkurve Collaboration 2018) to download the *TESS* target pixel files for NOI 105872 filtered using the SPOC quality flag QUALITY = 0 (J. M. Jenkins et al. 2016; J. Smith et al. 2020). Pixel-level aperture was constructed as a two-tier mask: background pixels were defined as the 30 per cent lowest-flux pixels in a reference cadence, while target pixels were selected using a threshold mask applied to the summed flux across cadences. The target flux was computed by summing all pixels in the target aperture and subtracting the median background flux per pixel multiplied by the number of target pixels. The flux uncertainties were estimated using the median absolute deviation of the simple aperture photometry SAP flux or the summed background, providing robust per-cadence error estimates. To remove long-term trends while preserving transit signals, the light curve was split into segments when gaps exceeded 2.4 h, corresponding to spacecraft data downloads and SPOC-flagged regions. Each segment was normalized individually and subsequently smoothed using an iterative Savitzky–Golay filter (five iterations with a 3σ clipping threshold) and a 48 h window size, which efficiently removes stellar activity while setting an upper limit on the duration of detectable transit events (A. Savitzky & M. J. E. Golay 1964; S. Hattori et al. 2022).

Currently there are data for NOI 105872 within Sector 6 and Sector 32 of the *TESS* observations. The Sector 6 data were taken between 2018 December 15 and 2019 January 06, and the Sector 32 data was taken between 2020 November 20 and 2020 December 16, with the Sector 32 data having a higher cadence (20 s cadence) than previously observed in Sector 6 (2 min cadence). Sector 6 has a greater transit depth than Sector 32, 13 per cent compared to 8.5 per cent, and we present all of the *TESS* photometry in Epoch 2 and 4 of Fig. 2(b).

2.3 SAAO

The South African Astronomical Observatory (SAAO), has a number of research themes, one of which is the search for and characterization of transiting exoplanets. NOI 105872 was observed at the SAAO 1m with the Sutherland High Speed Optical Camera (SHOC, specifically SHOC 'n' Awe; R. Coppejans et al. 2013) on 2020 January 03 in the I filter with 60 s exposures. The data were bias and flat field corrected via the standard procedure, using the SAFPHOT PYTHON package.[1] SAFPHOT was also used to carry out differential photometry, by extracting aperture photometry from the target as well as comparison stars using the 'SEP' package (K. Barbary 2016). SEP also measured and subtracted the sky background, adopting a box size and filter width which minimized the background residuals measured across the frame after the stars had been masked out. A few comparison stars in the 2.85 arcmin × 2.85 arcmin field of view were used to perform differential photometry on the target.

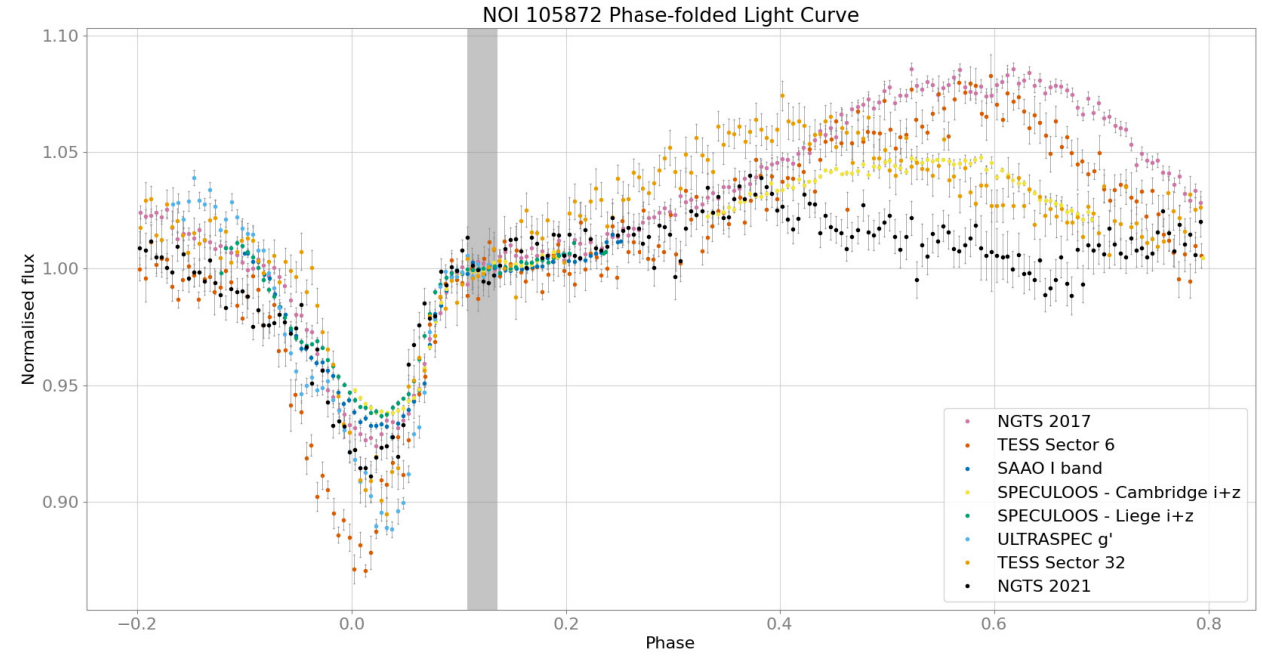
This was a targeted observation that lasted almost 6 h in total, but was ended prematurely due to high humidity at the observatory. Therefore, it only spans from phase −0.10 to 0.25, so does not include an out-of-eclipse observation. The maximum depth of the SAAO lightcurve is 7 per cent, and it can be seen in Epoch 3 of Fig. 2(b).

2.4 SPECULOOS

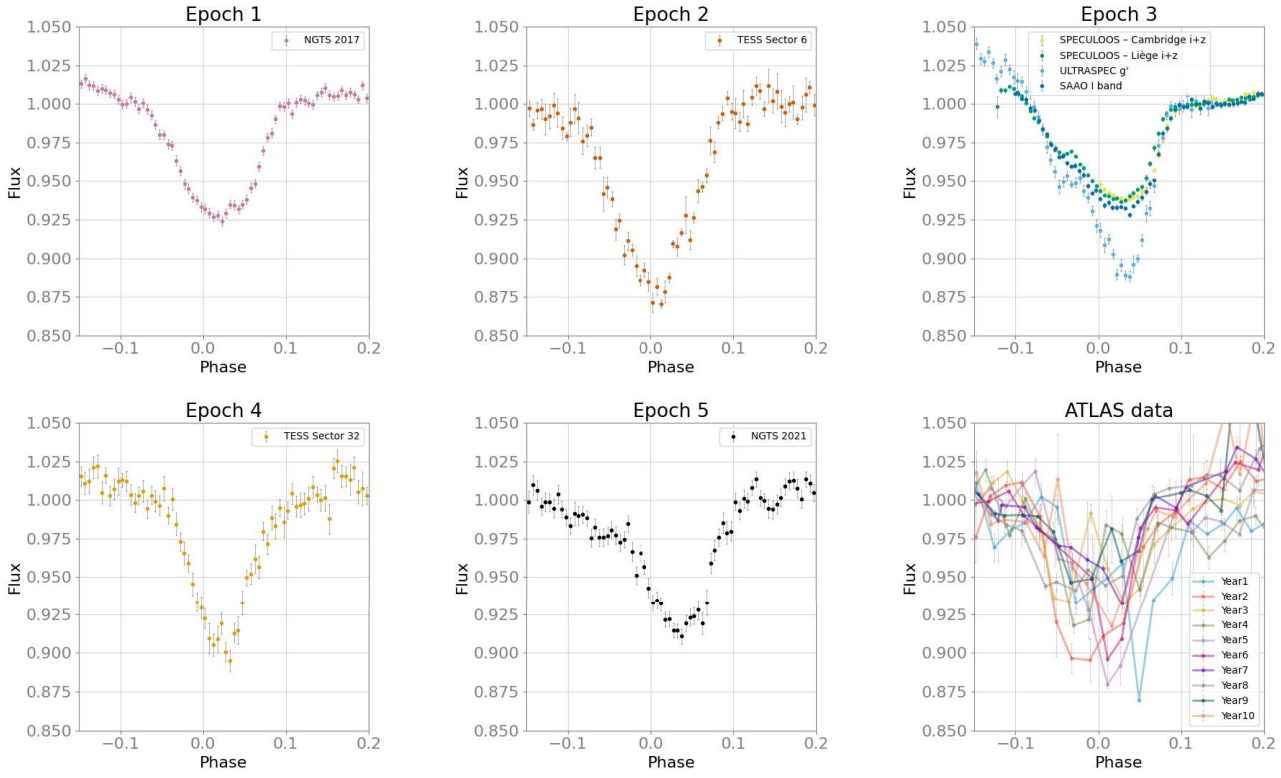
The Search for habitable Planets EClipsing ULtra-cOOl Stars (SPECULOOS) is a network of 1m telescopes across the globe (ESO Paranal Observatory in Chile, Teide Observatory in Tenerife and San Pedro Mártir observatory in Mexico) that aims to find

[1] https://github.com/apchsh/SAFPhot

Downloaded from academic.oup.com/mnras/article/552/3/stag1802/8834030 by University of Sheffield user on 29 October 2026



(a) Normalised phase plot



(b) Phase-folded light curves for each data set shown as a progression over time

Figure 2. Normalized eclipse light curves of NOI 105872 as a function of orbital phase, observed by a variety of different telescopes (see the legend). These data sets span 5 yr and display significant variability in both the eclipse depth and phase-curve shape. The shaded grey region shows the data range that was used to normalize the light curves. This region was chosen because the variation in gradients between the different data sets was the smallest. The data are also binned into 200 data points for each telescope data set. Sub-figure (b) show the progression of the eclipse light curve with each epoch of observation.

Downloaded from academic.oup.com/mnras/article/552/3/stag1802/8834030 by University of Sheffield user on 29 October 2026

transiting exoplanets around ultracool dwarf stars (L. Delrez et al. 2018; M. Gillon 2018).

The SPECULOOS observations were taken using the Callisto telescope in Chile between 2020 January 28 and 2020 January 29 in the *i* and *z* bands, and have a similar maximum eclipse depth as the SAAO data, taken a few weeks before, at ∼ 7.5 per cent. The data were reduced as per C. A. Murray et al. (2020). In Epoch 3 of Fig. 2(b), the SPECULOOS data are split into two sets, Cambridge and Liège. These represent the same data; however, they have been reduced by two different institutional pipelines and we have included both in this paper for completeness.

2.5 ULTRASPEC

ULTRASPEC is a high-speed imaging photometer mounted on the 2.4 m Thai National Telescope (TNT) at the Thai National Observatory (V. S. Dhillon et al. 2014). ULTRASPEC offers a selection of broad and narrow-band filters covering the optical range, with a typical field of view of approximately 7.7 × 7.7 arcminutes when using the full frame.

The full ULTRASPEC eclipse of NOI 105872 was observed on 2020 February 02 using the g' filter. Something of note is that the ULTRASPEC light curve is a lot deeper (11.5 per cent) than SAAO and SPECULOOS, even though they are taken within a few weeks of each other, as seen in Epoch 3 of Fig. 2(b). These features will be discussed in Section 2.7.

2.6 ATLAS

The Asteroid Terrestrial-impact Last Alert System (ATLAS) is a ground-based telescope survey consisting of two independent units situated on Hawaiian islands (J. L. Tonry et al. 2018). The telescopes have three filters, cyan (420–650 nm), orange (560–820 nm), and red (560–975 nm), so overall, the wavelength coverage ranges from around 400 to 1000 nm. ATLAS was designed as an all-sky survey to discover changes in light curves that signify moving or variable objects, such as asteroids or supernovae, and hence also lends itself to the detection of eclipsing stars or planets. It is for this reason that we looked at the ATLAS database to see whether eclipses of NOI 105872 had been captured. We accessed the ATLAS database through the Forced Photometry server (L. Shingles et al. 2021).

The data points for this object observed using ATLAS are sparse, as it has a typical cadence of two days with four exposures over a one-hour period, but they give us a broad idea of how the eclipse changes over time. We chose to only use the data points from the orange filter due to the higher data quality for this filter. Furthermore, the 10 yr worth of data is valuable for tracking longer term changes, and therefore these data are mainly used to back-up the other higher cadence data that we have for these periods of time. Due to the long duration of the total observations, there are a range of eclipse depths quoted in Table 1. Since the ATLAS data spans around a decade, we sectioned the data into years, and this can be seen in Fig. 2b.

2.7 Initial photometry results

Fig. 2(a) shows the light curves for NOI 105872 taken with all of these facilities over the course of 5 yr. The orbital period of the object was determined using a Lomb–Scargle periodogram, with the period corresponding to the strongest peak in the power spectrum. The orbital period of this object was found to be 0.691 ± 0.005 d and is phase-folded with an epoch of 2458591.744 BJD. The eclipses vary and have depths ranging from 7 per cent to 13 per cent.

Table 2. Bisector inverse span (BIS) values for the main seven data sets included in this paper. These are used as a measure of asymmetry of the eclipses.

Telescope	BIS
NGTS (2017)	0.0039±0.0025
TESS Sector 6	0.0034±0.0072
SAAO	0.01856±0.0012
SPECULOOS	0.0228±0.0018
ULTRASPEC	0.0235±0.0024
TESS Sector 32	0.0033±0.0074
NGTS (2021)	0.0197±0.0069

These photometric data reveal a number of interesting features. The first is that the eclipse is asymmetric, with the ingress generally lasting longer than the egress, as well as being much deeper than a normal transiting exoplanet.

Secondly, the light curves (Fig. 2a) also display an increase in brightness towards orbital phases of ∼0.5 (approximately half an orbit after the eclipse). This feature also replaces any potential secondary eclipse that we might expect to see for an eclipsing object, which raises questions on the nature of the primary eclipse, as well as the nature and composition of the eclipsing object, perhaps causing some sort of reflection effect. Finally, we observe clear variability when we take a closer look at how the light curve changes over time, as seen in Fig. 2(b). One of the main differences is a feature that we see appear in the SAAO, SPECULOOS, and ULTRASPEC data: an increase in flux, or 'bump', in the ingress, as seen in Epoch 3, between phase −0.065 and −0.025. These observations were taken within a few weeks of each other, and whilst the bump is not immediately obvious in the SAAO data, from our modelling (as seen in Section 4.3.2) we can see the beginnings of this feature. For the bump to appear at the same phase in each light curve, the period and stellar rotation would have to be well matched. With good spectra we can try to measure this. The eclipses also appear to be changing in terms of depth (see Table 1) and level of asymmetry. Table 2 shows the Bisector Inverse Span (BIS) for each of the eclipses, with the code used for this being adapted from similar methods used to identify asymmetries in spectral lines. Positive values indicate that the ingress is slower than the egress; however, certain data sets (NGTS 2017 and both *TESS* sectors) have a relatively negligible asymmetry, while the other data sets show a clearer asymmetric trend. The fact that these values also change is further testament to the variability of the light curve. Together, all of these features paint a complicated picture that we need to disentangle and solve to be able to characterize this enigmatic object.

It should be noted that when normalizing the light curve we had to be careful due to its variable nature. Generally, when normalizing an eclipse we would mask out the eclipse and then use the out-of-eclipse part of the phase curve to find a weighted mean or median and divide the full light curve by this amount. In the case of NOI 105872, the out-of-eclipse flux is much more variable than a standard light curve. We therefore identified the phase range over which the gradient of the light-curve varied least across the different epochs. The phase range used for normalization was 0.1073–0.1355 and is shown by the grey bar in Fig. 2(a). We used the weighted average flux in this range to normalize each

Downloaded from academic.oup.com/mnras/article/552/3/stag1802/8834030 by University of Sheffield user on 29 October 2026

data set. Although this normalization is based on the post-egress region only, the pre-ingress region showed significant variation in the local gradient between data sets, which would introduce a data set-dependent bias into the normalization, and was therefore not included in the normalization.

3 SPECTROSCOPIC OBSERVATIONS & HOST STAR CHARACTERIZATION

3.1 HARPS

In order to better characterize the system, we obtained three spectroscopic observations using the HARPS (High Accuracy Radial velocity Planet Searcher) spectrograph, on 2019 December 24, 2019 December 26, and 2020 February 10, under ESO programme ID 0104.C−0588 (P.I Bouchy). HARPS is a fibre-fed, high-resolution échelle spectrograph mounted on the ESO 3.6 m telescope at La Silla Observatory (M. Mayor et al. 2003). Operating in the visible range (380–690 nm) at a resolving power of $R \approx 115\,000$, HARPS is optimized for precise radial velocity measurements with a typical radial velocity precision of $\sim 0.5\,\mathrm{m\,s^{-1}}$ (M. Barbieri 2023) for bright, slow-rotating stars, and a long-term stability better than $1\,\mathrm{m\,s^{-1}}$ (C. Lovis et al. 2006).

The spectra were obtained in the high-efficiency mode (EGGS), and with an exposure time of 2700 s for the first two spectra and 3600 s for the third spectrum from 2020. HARPS is a fibre-fed spectrograph which enables the user to either monitor a wavelength calibration source or the sky brightness, simultaneously to a science observation. For a faint and fast-rotating source like NOI 105872, it is advantageous to place fibre B on-sky as we are limited by photon noise and not wavelength stability.

We accessed the raw data through the ESO data Archive and used the publicly available Data Reduction pipeline espdr version 3.3.9, for the extraction of the spectra, sky-subtracting, telluric correction, and wavelength calibration. The resulting spectra all have low SNR of respectively 4, 3 and 7 per pixel at 551 nm. The one observation in 2020 has a higher SNR, partly due to a slightly longer exposure time, but mainly attributed to moon contamination, which is clearly seen in fibre B. Using the binary masks available as part of the official pipeline, we cross-correlated the spectra with G2, K0, K5, and M2 masks on a wide CCF window of $\pm 250\,\mathrm{km\,s^{-1}}$, which all produce noisy CCFs which are insufficient to properly constrain the stellar velocity and mass of the orbiting object. The observations were taken at orbital phases 0.63, 0.33, and 0.77, respectively, and so none of them fall within the eclipse itself. Even if these spectra were of a reasonable SNR value, there is not a sufficient sampling across the phase curve to do any analysis on the changes in spectral line profiles.

Due to the very low SNR nature of the spectra, we also performed our own sky subtraction: rather than direct subtraction of the spectra, we needed to perform a scaling because these spectra from the sky and science fibres will not be exactly the same. The strength of the contaminant features needed to be scaled so that they are the same for both fibres and then a subtraction could be performed to completely remove the features not coming from the object we are interested in. To do this, first, we found strong contaminant features within the stellar and sky spectra, in this case, emission features at 5577 and 6300 Å. We fit a Gaussian to these lines and then used the amplitudes to create a subtraction coefficient (S) between the two spectra by taking the ratio of the amplitude of the line in the science fibre to the amplitude of the line in the sky fibre, and found the average of the two emission lines. This coefficient was then multiplied by the sky flux and subtracted from the science spectrum. The contaminant features are time-variable and so this process is completed separately for each spectrum. The sky-corrected spectra around the H α and Na doublet can be seen in Fig. 3.

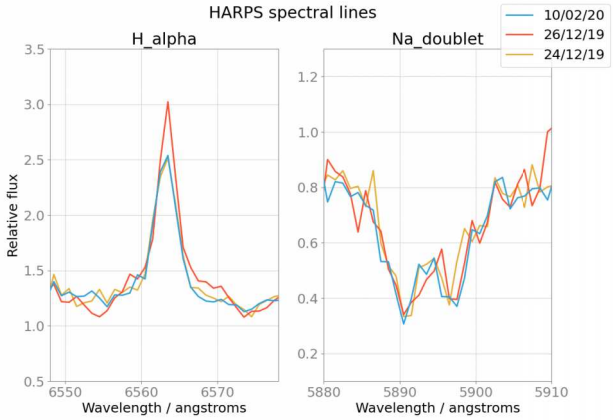


Figure 3. H α emission and Na doublet absorption features in the three HARPS spectra. These observations have been sky-subtracted and binned into 1 Å chunks.

3.2 Stellar characterization

In order for us to fully understand the object, we need to understand the host star first. The target star is a confirmed member of the Orion Nebula Cluster (ONC) (M. Kounkel & K. Covey 2019). We combine spectral diagnostics and spectral energy distribution (SED) modelling to constrain its fundamental properties.

We performed the initial SED fitting using the ASTROARIADNE package (J. I. Vines & J. S. Jenkins 2022), and then refined those values by using them to complete an isochrone fit with ASTROLACHESIS (Vines et al. submitted to A&A, 2026), results of which can be seen in Fig. 4 and Table 4. In the ASTROARIADNE code, there is an initial model filtering process based on initial values for things like the effective temperature. In this case the NextGen stellar atmosphere model (P. H. Hauschildt, F. Allard & E. Baron 1999) was the only model left after this internal filtering process. The errors found are based on the single-grid fit, and so are less realistic than that of a full multigrid search. The stellar parameters considered here place the object firmly in the regime of low-mass pre-main-sequence stars. The effective temperature corresponds to an approximate spectral type of M1–M2, while the combination of relatively low mass and inflated radius indicates that the star has not yet reached the main sequence, and is instead still contracting towards the main sequence.

The SED fit yields a distance of 371.7 pc, consistent with the distance inferred from the Gaia parallax (2.6315 mas; d ≈ 380 pc).

When placed on a Hertzsprung–Russell diagram according to the effective temperature and luminosity, this position lies above the main sequence and is consistent with evolution along a Hayashi track, characteristic of fully convective pre-main-sequence stars (C. Hayashi 1961). This is further supported by the young age (4.1 Myr), which is well within the contraction phase for a $\sim 0.4\ \mathrm{M}_{\odot}$ star (e.g. I. Baraffe et al. 2015).

Membership in the ONC reinforces this interpretation. The ONC is a well studied, very young star-forming region containing a large population of low-mass, pre-main-sequence objects (L. A.

Downloaded from academic.oup.com/mnras/article/552/3/stag1802/8834030 by University of Sheffield user on 29 October 2026

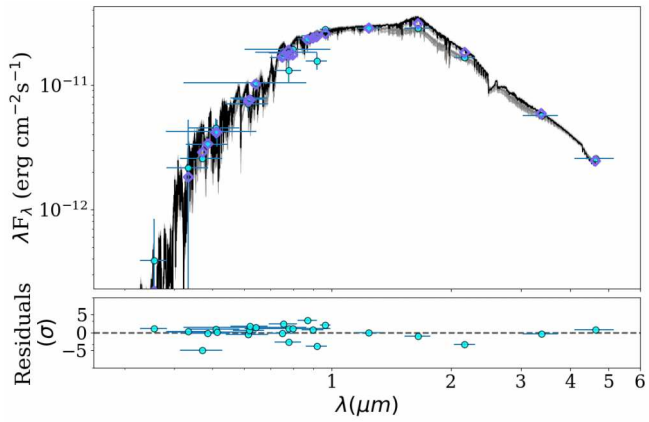


Figure 4. Spectral energy distribution of NOI 105872. Circles show the observed photometry (Table 3), diamonds show the corresponding synthetic fluxes from the best-fitting model. The solid line is the best-fitting NextGen stellar atmosphere model (P. H. Hauschildt et al. 1999), with shaded lines showing a sample of models drawn from the posterior distribution to illustrate the fit uncertainty, obtained using the ASTROARIADNE package (J. I. Vines & J. S. Jenkins 2022). Best-fitting parameters are given in Table 4. The lower panel shows the residuals in units of the photometric uncertainty.

Table 3. Magnitudes of the host star.

Band	Value	Source
u	19.747±0.038	SDSS
g	17.380±0.005	SDSS
r	15.904±0.004	SDSS
i	14.854±0.004	SDSS
z	14.224±0.004	SDSS
g	17.071±0.007	PanSTARRS
r	15.874±0.003	PanSTARRS
i	14.750±0.004	PanSTARRS
z	14.317±0.001	PanSTARRS
y	14.012±0.005	PanSTARRS
g	16.756±0.012	SkyMapper
r	15.875±0.027	SkyMapper
i	14.671±0.013	SkyMapper
z	14.179±0.006	SkyMapper
BP	16.727±0.014	*Gaia* DR2
G	15.463±0.004	*Gaia* DR2
RP	14.348±0.008	*Gaia* DR2
TESS	14.356±0.012	*TESS*
J	12.828±0.026	2MASS
H	12.042±0.021	2MASS
K	11.864±0.021	2MASS
WISE 3.4 micron	11.728±0.024	*WISE*
WISE 4.6 micron	11.609±0.021	*WISE*

Hillenbrand 1997). Stars in this environment are typically magnetically active, rapidly rotating to moderate degrees, and often exhibit strong surface inhomogeneities such as starspots and, in some cases, accretion hotspots.

No infrared excess is detected in the SED, indicating the absence of a primordial inner circumstellar disc, our observations do not go to long enough wavelengths to constrain middle/outer disc material. In the SED fit, we fix the metallicity value at Fe/H = 0.0, as seen in Table 4. The metallicty of the ONC usually sits around -0.01 ± 0.04 (V. D'Orazi et al. 2009). It should also be noted that due to the low SNR of the spectra, we cannot get a constraint of the metallicity spectroscopically and so the only way to find it is numerically from the photometry values. This is why we decided to fix it at a solar metallicity value.

The optical spectrum shows signs of Li I λ6708 Å (see Fig. A1) in absorption, a well-established indicator of stellar youth in low-mass stars, as lithium is rapidly depleted during pre–main-sequence evolution (P. Bodenheimer 1965; R. D. Jeffries et al. 2017). The spectrum also exhibits absorption from the Na I D doublet at ∼ 5890 Å (Fig. 3), together with prominent Ca I absorption features at λ6102 and λ6122 Å (see also Fig. A1). These features are shown as examples of the quality of our spectra and are just other photospheric lines that are visible despite the low SNR.

Balmer lines are detected in emission in the spectrum, indicative of elevated chromospheric activity commonly observed in young M-type stars. The Hα emission line can be seen in Fig. 3. Given the absence of an infrared excess, these features are attributed to magnetic activity rather than ongoing disc accretion (R. J. White & G. Basri 2003; M. Fang et al. 2009). The spectrum also exhibits emission from N II and O I. These lines cannot originate in the stellar photosphere at the effective temperature of the source ($T_{\rm eff} \simeq 3574$ K), as the ionization energies required are far in excess of those produced by a cool M-type star. Instead, these features are most naturally explained as contamination from the surrounding Orion H II region, which is known to produce strong nebular emission lines that are frequently superposed on stellar spectra in the ONC (J. A. Baldwin et al. 1991; D. E. Osterbrock & G. J. Ferland 2006; N. Da Rio et al. 2009).

In summary, the combined spectroscopic and photometric evidence identifies the source as a young (4.1 Myr), inner discless pre-main-sequence M1–M2 star in the Orion Nebula Cluster, with chromospheric activity typical of weak-lined T Tauri stars and superposed nebular emission originating from the surrounding H II region.

4 MODELLING AND INTERPRETING THE SYSTEM

In this paper, our analyses focus on the depth/asymmetry and variability of the eclipse, however we need to take into account the increase in out-of-eclipse flux when considering the full picture of models and hypotheses. A number of hypotheses were then explored for NOI 105872 to help us explain these features and fully characterize the object. These hypotheses are laid out below and summarized in Table 5.

4.1 Caused by the star

4.1.1 Stellar activity

Stellar activity, particularly in the form of dark starspots or bright plages, can significantly distort eclipse light curves. When an eclipsing companion crosses over a cooler, darker starspot, the amount of flux blocked by the companion is reduced, because the companion is blocking dimmer regions. This results in a temporary positive 'bump' in the eclipse profile (M. Oshagh et al. 2013; A. Valio 2017). Models show that such spot occultations by a companion generate identifiable anomalies whose magnitude increases when the spot is closer to the stellar disc centre

Downloaded from academic.oup.com/mnras/article/552/3/stag1802/8834030 by University of Sheffield user on 29 October 2026

Table 4. Stellar properties of the host star. The parameters from ASTROLACHESIS were determined in the modelling for this paper. The results, and therefore errors, produced for this paper are entirely numerical and do not take into account systematic errors. We urge the reader to take this into account when reading these figures.

Property	Value	Source
NGTS designations	NGTS J053956.4−042013 NOI 105872	
GAIA designation	*Gaia* DR3 3 023 459 583 984 210 304	
2MASS designation	2MASS J05395645-0420140	
TESS designation	TIC 11 356 619	
α (°)	84.985216	GAIA DR3
δ (°)	−4.337223	GAIA DR3
Parallax (mas)	2.6315±0.0379	GAIA DR3
Distance (pc)	$371.7^{+4.6}_{-4.9}$	astroLACHESIS
$T_{\rm eff}$ (K)	3574^{+45}_{-34}	astroLACHESIS
$\log g\,({\rm cm\,s^{-2}})$	3.99±0.03	astroLACHESIS
$A_{\rm V}$ (mag)	$0.197^{+0.199}_{-0.132}$	astroLACHESIS
R_* ($R_\odot$)	1.10±0.03	astroLACHESIS
M_* ($M_\odot$)	$0.42^{+0.03}_{-0.02}$	astroLACHESIS
L_* ($L_\odot$)	$0.17^{+0.03}_{-0.02}$	astroLACHESIS
Fe/H [dex]	0.00	Fixed
Age (Myr)	4.1±0.4	astroLACHESIS

Table 5. Proposed explanations for the eclipse of NOI 105872. Inspired by the table in T. J. David et al. 2017.

Hypothesis	Supporting evidence	Conflicting evidence	Conclusion
Stellar activity	Asymmetrical and variable eclipse, with bumps in the profile	Short-lived activity could be a factor influencing the variability, but unable to account for the overall eclipse shape–should be taken into account in tandem with other hypotheses	Not major contributing factor
'Dipper' stars	Deep, asymmetrical and variable eclipse	Less variable than usual dipper behaviour–no evidence of IR excess from the SED fit to indicate protoplanetary disc	Highly unlikely
Gravity darkening	Asymmetrical eclipse light curve	Models unable to produce the same eclipse morphology, don't take into account variability, and convective envelope implies weaker gravity darkening component	Highly unlikely
CPVs	Variable eclipse light curve and young M type host star	Morphology and its associated variability much more complex than our object	Unlikely
Magnetospheric clouds	Variable eclipse light curve	Short-duration, lack of accretion indicators, and unknown source of replenishment	Somewhat likely
Highly eccentric orbit	Asymmetrical eclipse light curve	Does not account for the variability of the eclipse profile	Not a major contributing factor
Evaporating planet	Deep, asymmetrical and variable eclipse	Mass-loss rate would have to remain relatively constant and not be affecting the orbital alignment	Highly unlikely
Tilted disc system	Deep, asymmetrical and variable eclipse	Models line up well; variability can be explained through precession of the disc and effects of stellar activity on the disc, asymmetry due to the tilted nature of the system	Most likely

and depends on the spot's size (filling factor) and temperature. These anomalies can bias key eclipse measurements, such as depth, duration, and timing, and in the case of exoplanets leads to underestimates in planet radius by a few percent and causing transit timing variations (TTVs) up to several minutes (C. A. Watson & V. S. Dhillon 2004; S. C. C. Barros et al. 2013; P. Ioannidis, K. F. Huber & J. H. M. M. Schmitt 2015). Over multiple eclipses, evolving starspot positions, and their relationship to the orbital and rotational periods, can shift the phase of these bumps, producing asymmetries and time-dependent variability in the light curve, including mid-eclipse asymmetry and apparent shifts in the ingress and egress (R. Sanchis-Ojeda et al. 2011; S. C. C. Barros et al. 2013). More extreme, long-lived cases, such as TOI-3884, show a massive polar starspot covering about 17 per cent

Downloaded from academic.oup.com/mnras/article/552/3/stag1802/8834030 by University of Sheffield user on 29 October 2026

of the stellar surface, causing distinct double-bump patterns and strongly asymmetric transits due to the companion's unconventional pole-crossing orbit (J. M. Almenara et al. 2022).

It is unlikely in the case of NOI 105872 that stellar activity is the cause of our asymmetric light curve. Short-lived stellar activity, such as starspots, could however cause some features that we see, such as the ingress 'bump' in Fig. 2(b). Unocculted starspots would also help to explain why the ULTRASPEC eclipse is much deeper than the other two data sets in Fig. 2(b). This is because starspots are cooler material and so emit much less blue light than red, hence appear especially dark at bluer wavelengths. If some of these spots are not crossed by the companion during an eclipse, they reduce the star's overall brightness, particularly in blue light, while the companion still blocks the same amount of the stellar surface. This makes the drop in light during the transit look larger than it really is, so the transit appears deeper in blue wavelengths compared to red. Another effect could be the sinusoidal nature of the out-of-eclipse part of the phase curve. While this could be associated with starspots and faculae, these events alone could not explain the overall eclipse curve which shows asymmetry and great eclipse depth over the course of 4 yr. Long-lived stellar activity, such as the polar spot in J. M. Almenara et al. (2022), would be too stable to give the variability in the eclipse curve. The conclusion here is that stellar activity should be taken into account in any further analyses, but does not explain the key features of the light curve.

4.1.2 'Dipper' stars

'Dipper' stars are a type of young stellar object (YSO) and subclass of T Tauri stars that exhibit dimming events that can be episodic or quasiperiodic. These events can cause the brightness to drop by $\sim$ 10 per cent–50 per cent (e.g. S. H. P. Alencar et al. 2010; M. Ansdell et al. 2016; J. E. Rodriguez et al. 2017; A. M. Cody & L. A. Hillenbrand 2018; N. Roggero et al. 2021). While the light curve of our object shows a deep dimming (up to $\sim$ 13 per cent), asymmetric ingress/egress, and a multi-year stability over $\geq$ 10 yr, these features differ in several respects from classical 'dipper' stars. Dippers in star-forming regions (e.g. Taurus, Upper Sco, etc.) have dips that are usually highly stochastic or quasi-periodic, with large variation from epoch to epoch in depth, duration, shape, or interval. For example, N. Roggero et al. (2021) find that among disc-bearing young stars $\sim$ 30 per cent show dipper behaviour; many are aperiodic, most show changing structure on time-scales of one rotation, and dip depths and shapes vary substantially. By contrast, our object maintains a reproducible shape (including asymmetry) over many years; moreover, unless other diagnostics point to a protoplanetary disc (as noted earlier, we see no signs of an IR excess), we have no evidence for the typical protoplanetary disc environment that dipper models require. Therefore, although superficially similar in some respects, the evidence strongly suggests that this object's occulting structure is likely due to a different geometry.

4.1.3 Gravity darkening

Gravity darkening occurs when changes in local effective gravity cause flux variations across the stellar surface and, in the case of rapidly rotating stars, this leads to darker equatorial regions and brighter poles (H. Zeipel 1924; F. Espinosa Lara & M. Rieutord 2012). An object transiting in front of a gravity darkened host star will produce an asymmetric or differently shaped light curve (J. W. Barnes 2009; S. Dholakia, R. Luger & S. Dholakia 2022). Structural and environmental properties have important implications for the expected strength of gravity darkening. In classical formulations, gravity darkening follows the von Zeipel relation (H. Zeipel 1924), in which the local effective temperature scales with surface gravity as $T_{\rm eff} \propto g^{\beta}$, with $\beta \approx 0.25$ for stars with radiative envelopes. However, this prescription does not apply to early M type stars that have a convective envelope. More appropriate treatments (e.g. L. B. Lucy 1967) show that convective envelopes yield significantly smaller exponents ($\beta \approx 0.08$ or lower), resulting in substantially weaker surface temperature gradients even in the presence of rotationally induced gravity variations. We still modelled the object orbiting a gravity darkened star to see if the shape of the light curve could be explained in this way. We built a custom code to model this for a range of stellar and orbital orientations.

To test whether the observed eclipse morphology could be reproduced by a planet orbiting a gravity-darkened star, we constructed a simple three-dimensional model of a transit across an oblate stellar photosphere. The model is intended as a qualitative, proof-of-concept framework rather than a fully self-consistent treatment of stellar structure or orbital dynamics.

The stellar surface is represented as an oblate spheroid defined on a spherical polar grid (θ, ϕ). Here, θ is the colatitude measured from the stellar rotation axis (such that $\theta = 0$ at the North pole and $\theta = \pi/2$ at the equator), and ϕ is the azimuthal angle in the equatorial plane. In Cartesian coordinates the surface is described by

$$x = R_\star \sin\theta \cos\phi, \quad (1)$$
$$y = R_\star \sin\theta \sin\phi, \quad (2)$$
$$z = R_\star (1 - f) \cos\theta, \quad (3)$$

where $R_\star$ is the equatorial radius and f is an oblateness parameter describing fractional polar compression. The surface is discretized on a uniform angular grid. To allow arbitrary viewing geometries, the stellar surface is rotated via successive Euler rotations, enabling independent specification of the stellar inclination and sky-projected orientation.

Gravity darkening is implemented using a simplified, latitude-dependent parametrization. In a physically self-consistent treatment, the local effective temperature is related to the effective surface gravity via the von Zeipel relation,

$$T_{\rm eff} \propto g_{\rm eff}^{\beta}, \quad (4)$$

where β is the gravity-darkening exponent and which implies a local flux scaling

$$F \propto g_{\rm eff}^{4\beta} \quad (5)$$

The effective gravity itself depends on latitude through the combined gravitational and centrifugal potentials, and must be computed from a Roche model for a rotating, oblate star (e.g. H. Zeipel 1924; F. Espinosa Lara & M. Rieutord 2012).

In this work, we do not attempt to compute $g_{\rm eff}(\theta)$ self-consistently. Instead, we adopt a simple analytic prescription in which the surface brightness varies smoothly between the poles and equator according to

$$I_{\rm grav} \propto |\cos\theta|^{\beta}, \quad (6)$$

where θ is the colatitude measured from the stellar rotation axis. This form reproduces the qualitative behaviour expected from gravity darkening, namely brighter poles and a dimmer equator,

Downloaded from academic.oup.com/mnras/article/552/3/stag1802/8834030 by University of Sheffield user on 29 October 2026

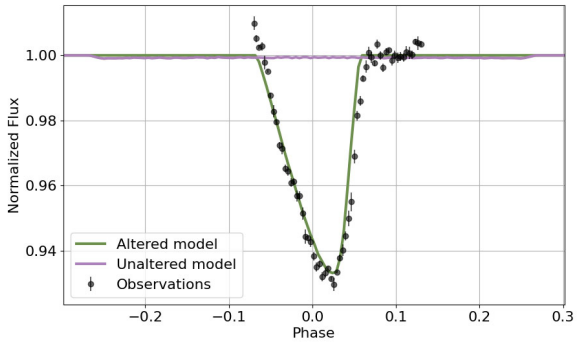


Figure 5. 3D gravity darkening model for two scenarios overplotted with the SAAO observations for NOI 105872. There is an unaltered model which represents the model if we use the calculated orbital separation and correct gravity darkening exponent (0.08) which is shown in purple. The model in green is provided as an example and not a true fit to the data. The parameters adopted to get a reasonable fit are in Table 6, and are significantly different to the known, measured or expected parameters of the system. This includes using a value of $\beta = 0.25$ rather than 0.08 as would be expected for this kind of star. To adopt reasonable parameters the model differs significantly from the observed data.

while avoiding the need for a full treatment of the stellar potential. The exponent β therefore acts as an effective parameter controlling the strength of the latitudinal brightness contrast, rather than a direct physical mapping to the von Zeipel coefficient. Limb darkening is included using a quadratic law, defined by u_1 and u_2. The final intensity map is constructed as a weighted combination of $I_{\rm grav}$ and $I_{\rm limb}$ and normalized to unity in the absence of occultation.

The companion is modelled as an opaque spherical body of radius $R_{\rm p}$ moving along a linear trajectory across the projected stellar disc. The orbital inclination and semi-major axis determine the impact parameter, while a sky-projected spin-orbit misalignment angle, λ, is introduced by rotating the transit chord relative to the stellar rotation axis.

At each time-step, surface elements whose projected separation from the planet centre satisfies

$$d \leq R_{\rm p} \tag{7}$$

are treated as occulted. The observed stellar flux is computed by summing the intensities of all visible, unocculted surface elements and normalizing by the unobscured stellar flux.

The model neglects several physical effects, including differential rotation, self-consistent computation of surface gravity, wavelength-dependent limb darkening, finite exposure-time integration, and full Keplerian orbital motion. Nevertheless, it captures the principal geometric and photometric consequences of transiting an oblate, gravity-darkened star.

Fig. 5 shows a sample of the gravity darkening model over the SAAO observational data set. We provide this as an example for how the model can be used, but it should be noted that the already known parameters had to be changed for this model to more closely reflect the eclipse morphology of NOI 105872. The values input into the model can be seen in Table 6. In this table, θ represents the angle that the star is tilted up/down in our line of sight, and ϕ is the angle that the star is tilted left/right. Without allowing all of these variables to change, we could not find an appropriate fit through MCMC fitting. Most notably, the semi-major axis is much larger than our already calculated value of 0.011 au, and the gravity darkening exponent used is that of a radiative envelope ($\beta = 0.25$) to show a more extreme version of gravity darkening compared to what we would get with $\beta = 0.08$ of a convective star. We did try to run the model fit using $\beta = 0.08$, but the eclipse depth and shape could not be closely recovered. We can see that the asymmetric structures predicted by gravity darkening do not match the form of the measured light curve. From our modelling, along with the literature search, we therefore conclude that the observed eclipse shape is unlikely to arise from a planet orbiting a gravity-darkened star.

Table 6. Model input parameters for the 3D gravity darkening model.

Parameter	Value
$R_*(R_\odot)$	1.1
$R_{\rm p}(R_{\rm J})$	2.83
f	0.1
β	0.25
u_1	0.8
u_2	0.2
a(au)	0.069
$i(^\circ)$	84.9
$\lambda(^\circ)$	33.5
$\theta(^\circ)$	65
$\phi(^\circ)$	1.5

4.1.4 *Complex periodic variables (CPVs)*

Complex periodic variables (CPVs) are a class of young, rapidly rotating stars, typically late-type M dwarfs, that exhibit complex periodic light curves with periods generally shorter than a few days (J. Stauffer et al. 2017). Their photometric variability cannot be explained by starspots alone (J. Stauffer et al. 2017; Z. Zhan et al. 2019; C. Koen 2021), indicating the presence of additional structures or processes associated with the stellar environment. The leading explanations invoke spatially concentrated circumstellar material that corotates with the star (J. Stauffer et al. 2017; M. N. Günther et al. 2022). Proposed scenarios include dust clouds orbiting near the Keplerian corotation radius and periodically transiting the stellar disc (J. Farihi, T. von Hippel & J. E. Pringle 2017; H. Sanderson et al. 2023), as well as magnetically supported prominences consisting of cool, dense gas embedded within the stellar corona (A. Collier Cameron & R. D. Robinson 1989; M. Jardine & A. Collier Cameron 2019; R. F. P. Waugh & M. M. Jardine 2022). Both mechanisms can produce the complex and evolving eclipse-like features that characterize CPV light curves.

Recent studies have further established the observational properties of the CPV population (L. G. Bouma et al. 2024). CPVs are found predominantly among young M dwarfs with masses of approximately 0.1–0.4 $M_\odot$, while higher-mass hosts are comparatively rare. Their photometric periods are generally stable over time-scales of years, although the detailed light-curve morphology can evolve substantially during the same interval. CPVs are also frequently observed to exhibit superposed spot-modulation signals, producing an underlying quasi-sinusoidal component in addition to the more complex eclipse-like variability.

NOI 105872 shares some characteristics with known CPVs. In particular, its period appears stable over the two-year observing baseline, consistent with the behaviour reported by L. G. Bouma

Downloaded from academic.oup.com/mnras/article/552/3/stag1802/8834030 by University of Sheffield user on 29 October 2026

et al. (2024). However, its light-curve morphology is considerably simpler than that typically observed in CPVs, which often display multiple evolving dips and significantly more complex structures. Furthermore, the host star of NOI 105872 has a mass exceeding 0.4 $M_\odot$, placing it just outside the mass range occupied by the majority of known CPVs. While the CPV interpretation therefore cannot be ruled out entirely, the available evidence suggests that NOI 105872 is unlikely to be a typical member of this class.

4.1.5 Magnetospheric clouds

For certain stars, particularly high-mass stars, transiting circumstellar magnetospheric clouds are suggested to be a cause of photometric variability (D. Groote & K. Hunger 1982). The clouds consist of plasma which has been trapped in the magnetosphere of the star and appear most dense at the corotation radius (R. H. D. Townsend et al. 2013). For fully convective, low-mass pre-main-sequence stars, such as the host star NOI 105872, magnetic field strengths are generally in the range 0.1–1 kG (e.g. C. M. Johns-Krull 2007; J.-F. Donati & J. D. Landstreet 2009), which can cause charged material to become trapped in the magnetosphere once it enters an orbit about the star. Closed field lines around the corotation radius cause the material to settle at this point, forming a co-rotating cloud of plasma (e.g. A. Collier Cameron & R. D. Robinson 1989; J. Stauffer et al. 2015). This model has been invoked for a small but well-studied set of young, rapidly rotating stars exhibiting periodic, depth-variable flux dips synchronous with the stellar rotation period, including σ Ori E and RIK-210 (R. H. D. Townsend, S. P. Owocki & D. Groote 2005; T. J. David et al. 2017).

The variable eclipse depth observed in the light curve of NOI 105872 is qualitatively consistent with this scenario. In magnetospheric cloud models, recurrent processes remove dust and gas from the prominence while chromospheric evaporation replenishes gas from below (S. Daley-Yates & M. M. Jardine 2024), naturally producing long-term variability in the column density of occulting material and therefore in the eclipse depth. The period of 0.69 d further supports this interpretation, as slingshot prominences are a characteristic feature of rapidly rotating stars, with the canonical example being AB Doradus at a comparable rotation period of 0.514 d (A. Collier Cameron & R. D. Robinson 1989).

The asymmetric eclipse profile offers a further constraint on the cloud morphology. The variable morphology of dimming events in systems such as RIK-210 suggests that the occulting material is not a single, spherical body (T. J. David et al. 2017), and asymmetric profiles are expected when the leading and trailing edges of the cloud have different density gradients.

The magnetospheric cloud model does however face several difficulties in this system. The main issue is the lack of accretion indicators within the spectroscopy, which is not observed here. Furthermore, the long-term increase in eclipse depth between certain epochs implies that material is being periodically replenished on a time-scale of years. While the cyclic slingshot and replenishment process provides a qualitative explanation, the decade-long coherence of the signal is more consistent with a stable, long-lived structure than with the typically short-lived prominences seen on other rapidly rotating stars (A. Collier Cameron & R. D. Robinson 1989; S. Daley-Yates & M. M. Jardine 2024). Alternatively, the cloud could be precessing, such that the transiting portion of the cloud is different at each epoch. Overall, the magnetospheric cloud model is qualitatively consistent with several features of the light curve of NOI 105872 but is not modelled quantitatively here, and should therefore be considered with caution as one of several competing hypotheses.

4.2 Caused by the orbit

4.2.1 Eccentricity

One of the first causes for an asymmetric light curve that we hypothesized and tested was a companion on a highly eccentric orbit. Whenever transiting planets are on an eccentric orbit, the acceleration of the planet as it transits in front of its host star can cause changes in the ingress and egress, which therefore makes the light curve asymmetric (J. W. Barnes 2007).

We used the BATMAN PYTHON package (L. Kreidberg 2015) to model the eclipse light curve and ran an MCMC fit using EMCEE (D. Foreman-Mackey et al. 2013), allowing all of the following variables to change: radius of the object (R_p), semimajor axis (a), inclination (i), eccentricity (e), argument of periastron (ω), time of inferior conjunction (t_0), and a model offset that allows the level of the continuum to shift from 1. From this, we found the best fit for the BATMAN model for both *TESS* and both NGTS light curves, which can be seen in Fig. 6. The best-fitting parameters found from these fits are given in Table 7. We chose to fit the lightcurves at a range of ± 0.16 to the t_0 estimate for consistency, this range is large enough that it encapsulates all of the complete eclipses and includes some of the out of eclipse light as well. At first glance, the eccentricity model appears to fit the data quite well, however there are some caveats that we have to take into account. Firstly, the eccentricity model does not explain the increase in flux in the out-of-eclipse part of the light curve, and secondly, we still need to compare these fits to other models, such as the tilted disc model in Section 4.3.2. We can also see that certain values, such as the semimajor axis, vary between models and, in some cases, are not within errors of one another. It is unlikely that a parameter like this would vary significantly between epochs.

And so, high orbital eccentricity can be ruled out as the only contributing factor to the asymmetric light curve. This is not to say that an eccentricity in the orbit is not contributing to the asymmetry, but it will not cause all of the features that we see in the photometry.

4.3 Caused by the companion

4.3.1 Evaporating planet

When exocomets transit in front of a star, they produce a light curve just as a transiting exoplanet would. These light curves tend to be asymmetrical (I. Luk'yanyk et al. 2024). This is due to comets having a ribbon tail of ice and dust coming off of them, as well as a coma around the nucleus of the comet. This dust will block a portion of the light coming from the star as it passes after the comet, making the egress of the transit curve far more gradual than the ingress. This has also been seen to occur for particular exoplanetary light curves, such as KIC 12557548b (J. Budaj 2013), where a comet-like tail is observed to be following along after the planet. This could be attributed to the object having an accompanying variable dust cloud that could have originated from the disintegration of the object (M. Brogi et al. 2012).

Downloaded from academic.oup.com/mnras/article/552/3/stag1802/8834030 by University of Sheffield user on 29 October 2026

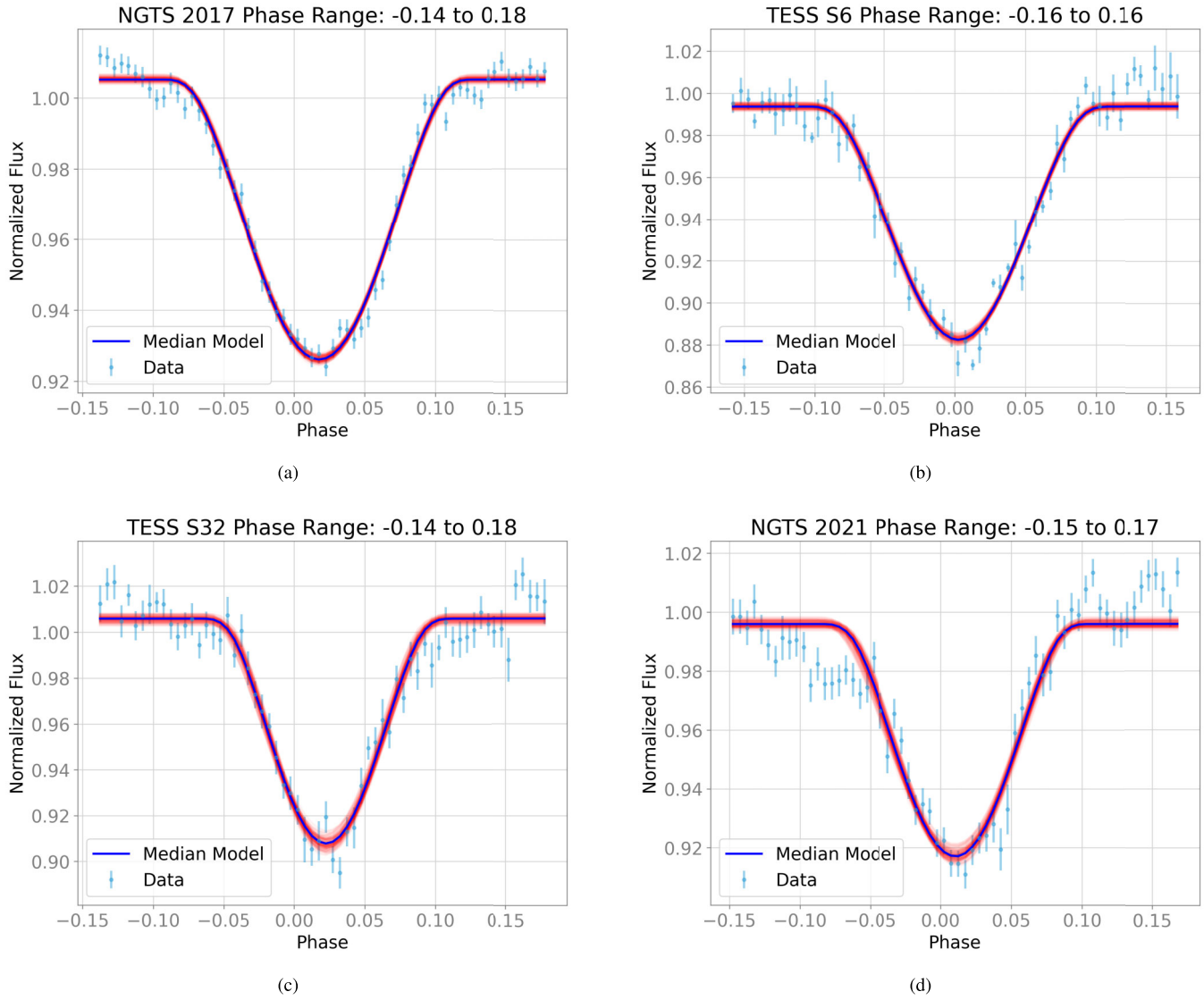


Figure 6. Best-fitting MCMC using BATMAN shown with a solid line, overplotted with the NGTS and *TESS* binned data points. The shaded lines represent the iterations of the MCMC model before the best fit is found.

Table 7. Results of MCMC fitting the batman model to the photometric phase curves for NGTS and *TESS*, along with the chi-squared value for each model fit.

Value	NGTS (2017)	*TESS* S6	*TESS* S32	NGTS (2021)
e	$0.484^{+0.011}_{-0.021}$	$0.469^{+0.023}_{-0.042}$	$0.446^{+0.038}_{-0.066}$	$0.467^{+0.025}_{-0.060}$
$\omega(^\circ)$	$280.4^{+6.5}_{-9.6}$	$270.4^{+12.3}_{-13.2}$	$264.1^{+21.6}_{-18.1}$	$278.5^{+13.0}_{-19.9}$
$R_p(R_J)$	$3.30^{+0.14}_{-0.06}$	$4.30^{+0.48}_{-0.38}$	$4.17^{+0.85}_{-0.54}$	$3.63^{+0.44}_{-0.30}$
$a(R_*)$	$2.18^{+0.05}_{-0.04}$	$2.39^{+0.09}_{-0.11}$	$2.68^{+0.18}_{-0.19}$	$2.45^{+0.13}_{-0.08}$
$i(^\circ)$	$75.39^{+0.57}_{-0.29}$	$75.82^{+0.97}_{-0.60}$	$76.15^{+1.48}_{-0.84}$	$75.78^{+1.37}_{-0.58}$
t_0	$0.021^{+0.002}_{-0.003}$	0.003±0.003	0.022±0.004	0.013±0.003
χ^2	131.2	295.2	161.9	215.5
BIC	160.3	324.3	191.0	224.6

However, in the case of NOI 105872, we can see in Fig. 2(b) that, in the epochs that are asymmetric, it is the ingress that is less steep than the egress, which means that if there were a ribbon tail of dust, it would have to be leading the object rather than trailing.

One of the causes of a leading cloud of dust around the object would be if the object's atmosphere is evaporating, or if the object itself is disintegrating as was the case with KIC 12557548b. This could occur due to the high irradiance of the atmosphere from the the activity of the host star. As radiation bombards the atmosphere, it expands past the object's Roche lobe and therefore is no longer bound to the object (G. Foster et al. 2022; V. Bourrier & A. Lecavelier des Etangs 2018). The light curve produced by NOI 105872 could also be considered reminiscent of disintegrating planets such as K2-22b (R. Sanchis-Ojeda et al. 2015). In this case, the mass-loss rate would have to be sustainable over the course of our observations, and consistently replenishing.

Downloaded from academic.oup.com/mnras/article/552/3/stag1802/8834030 by University of Sheffield user on 29 October 2026

Because dust lifetimes are short, stellar winds could not vary drastically or else the asymmetry may change significantly. The orbital alignment would also have to remain stable even as the object loses mass. It should also be noted that not all of the light curve epochs show the asymmetry that would be expected of an evaporating planet. Therefore, we note that the shape of the eclipse and long-term stability in this case are significantly different from systems like K2-22b, and so is unlikely to be an evaporating planet.

4.3.2 Tilted disc system

So far, we have discussed how the geometry of this system has to be relatively atypical for us to see the shape of the eclipse that has been observed, with the variability of the light curve being an added barrier for our models and hypotheses. It is entirely possible that this object is something far more complicated than what can be easily explained by a single hypothesis. Other objects that have very complex and unusual light curves include J1407b (M. A. Kenworthy & E. E. Mamajek 2015b) and ASASSN-21js (T. H. Pramono, M. A. Kenworthy & R. van Boekel 2024), both of which are unusually deep and asymmetric, and have since been modelled as giant exoring (rings around exoplanets, analagous to Saturn's rings) systems. Our object is too close to its host star to be a similar system, however perhaps these objects can give us an insight into the geometry and origin of our light curve.

This leads us to our most promising hypothesis so far; we considered a tilted disc around an eclipsing companion. The asymmetry of our light curve could be due to the tilted geometry of the disc system, with the depth of the eclipse being directly related to the radius of the disc around the object. With this hypothesis we can also explain the variability that is seen year upon year. There are two processes that could be causing this; precession and stellar activity. A disc precesses due to radiation, magnetic or gravitational influences on the system over time, and this seems especially likely when we consider how small the distance is between the object and its host star. Even if these changes are gradual, they will eventually cause changes within the eclipse profile. We have already discussed the young and active nature of the host M-star in this system, and how certain stellar activity events, such as star spots, can cause features like the ingress bump previously discussed. Other stellar activity events, such as flares and coronal mass ejections would cause the disc to be bombarded by radiation. Upon absorbing this radiation the disc could expand, or 'puff up', changing the size and opacity that is then noticeable within the light curve. A tilted disc composed of dust could also cause reflected light, which would help to explain the increase of flux in the out-of-eclipse part of the lightcurve.

We used a custom code to model a tilted disc orbiting in front of the star (M. A. Kenworthy & E. E. Mamajek 2015a, b). Once we created a preliminary fit by eye to the data, we developed MCMC fits for each of the light curves, using the package EMCEE (D. Foreman-Mackey et al. 2013), to ensure that the disc parameters were best-fit to the data. The free parameters within the MCMC fit were as follows: offset of disc from centre of star (y), inclination of disc in degrees (i) where $i = 90^\circ$ would be edge on, rotation of the semi-major axis from the x-axis (ϕ) where the x-axis is the horizontal line left to right along the star, radius of disc (r), transmission of disc (t_x), the point where the middle of the disc covers the star ($hjd_{\rm central}$) and a model offset that allows the continuum to shift from 1.

When performing the MCMC fits we had to choose carefully which of the data sets to use, especially because of the bump in the ingress that we have already discussed (see Fig. 2b); this excludes SAAO, SPECULOOS, and ULTRASPEC. Without taking stellar activity into account, the fits could be skewed by their effects on the light curve. There are two options for dealing with the ingress bump: (1) mask out the bump and fit the rest of the eclipse, or (2) simultaneously fit a stellar activity model that takes into account the bump while the rest of the eclipse is fit by the disc model. Masking out this bump would be difficult as the limits will be set by eye and this would not be completely accurate. If the fits for these data were needed in the future then an accompanying stellar activity model would need to be fit simultaneously. Instead, we choose to only fit the data to NGTS (2017), *TESS* Sector 6, *TESS* Sector 32, and NGTS (2021) due to their lack of any noticeable bump in the eclipse.

Upon initial fitting of the data it became clear that the NGTS (2021) light curve is likely also affected by stellar activity, in a similar way to the SAAO data where we did not pick up on the effects by eye, but noticed the change in ingress when we started fitting models to the data. Once the model was fit to the data, a small bump in the ingress became clear, as well as a lengthening of the eclipse duration, starting earlier than the rest of the light curves. These data were taken over the course of several months, so if we separate the data into small chunks, representing around 3–4 weeks at a time, and phase fold it, we can see that some of the chunks do not show as much stellar activity interference. We keep the tilted disc fit in as an example, to show how the effects of stellar activity change the model fit, and hence we still do not choose to fit the SAAO, SPECULOOS and ULTRASPEC data sets, the ones that exhibit the bump as shown in Fig. 2b.

Fig. 7 and Table 8 show the results of the MCMC fitting for the four remaining light curves. Each light curve is modelled over a phase range of ± 0.16 from the estimated t_0 value, the same range as the BATMAN models for direct comparison. Since we have already discussed the effect of stellar activity on the NGTS (2021) light curve, it is unsurprising to see that this fit is different from the others. Particularly, the increased eclipse duration will affect the radius of the disc needed to produce this shape, which is why the disc is much wider than in previous fits. Overall, though, the orientation and transmission of the disc is relatively similar to the other fits.

At first glance it might appear that the *TESS* Sector 32 fit is also different from the initial two; however, when we look at Table 8, we can see that most of the *TESS* Sector 32 model parameters are within the errors of the fits for NGTS 2017 and *TESS* Sector 6. This is with the exception of the transmission value, however we can also see that the value for ϕ is not constrained very well and so the fitted value of this could be affecting the transmission value. These values are linked because changing both the orientation and opacity of the disc will change the amount of light that is blocked coming from the host star so if they are unconstrained then it is difficult to determine which factor is affecting the eclipse curve more.

If we look at the NGTS 2017 and *TESS* Sector 6 data, the discs are incredibly similar, and most parameters are within errors of each other. This is very promising, especially since the two data sets are taken about a year apart and we would not expect to see many differences on those time-scales. The slight change in orientation could be representative of the disc precession that was previously discussed. Fig. 8 shows the same *TESS* Sector 6 data, this time we fit an inner disc similar to the initial fits, but with an

Downloaded from academic.oup.com/mnras/article/552/3/stag1802/8834030 by University of Sheffield user on 29 October 2026

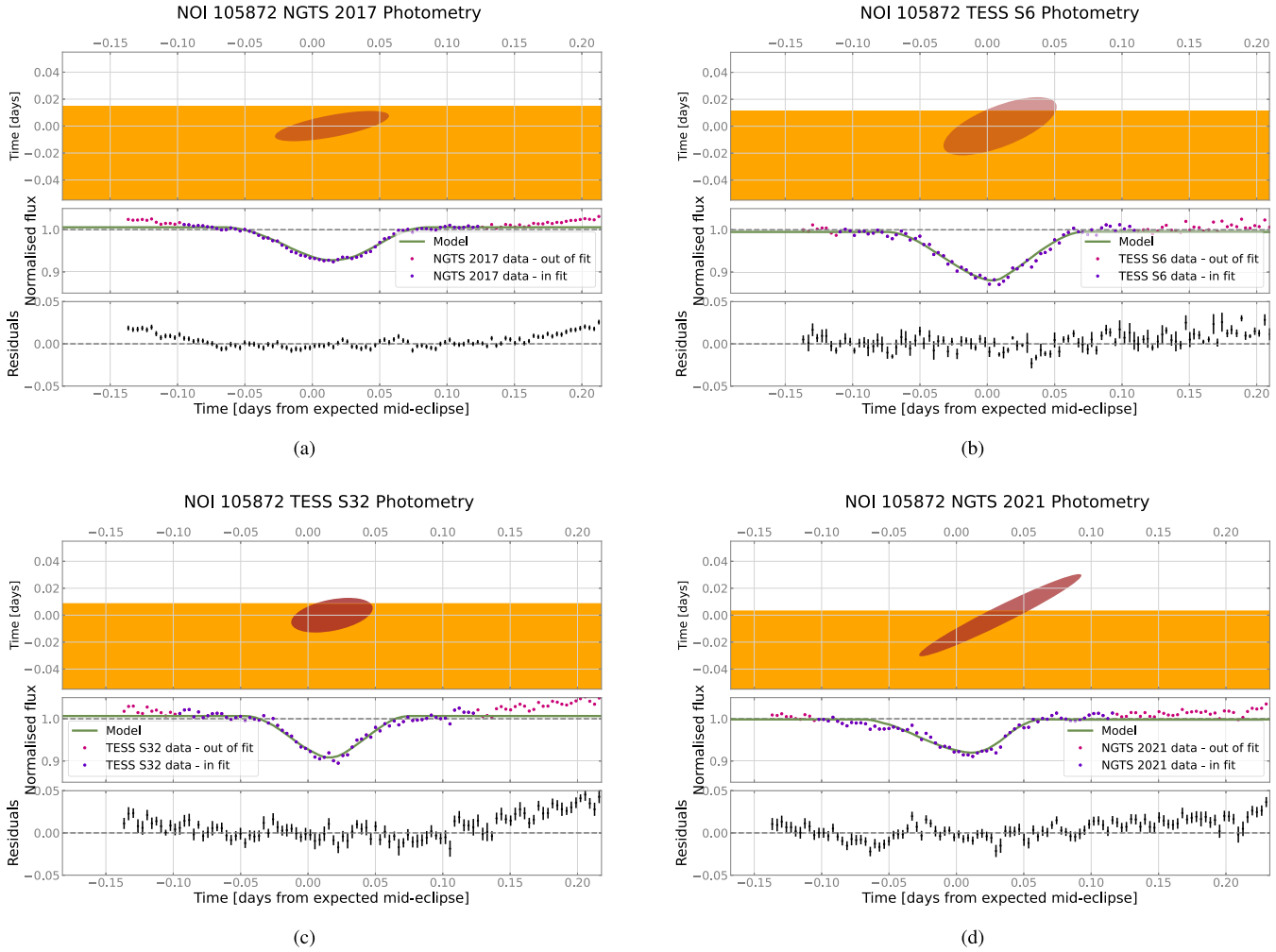


Figure 7. Tilted disc models for four of the data sets of NOI 105872 after MCMC fitting. The green line represents the model with parameters found from the MCMC fits, and the circles are the actual binned data points from the phase-folded light curves of the respective telescopes, multiplied by the period to convert it into time. The purple circles represent the datapoints that were used to fit the tilted disc model and the pink circles are for the data that were not used in the fit. The yellow band represents the top centre of the star across time, with the width of the band being an arbitrary amount of time so that the band fills the length of the plot area, and the height being the diameter of the star in days. The starting y co-ordinate for the rectangle is $(y - dstar/2)$ so the offset of the top of the star to 0.0 on the y-axis is the modelled y value in days. We are mostly concerned with seeing how the disc covers the star at time of mid-transit. The opacity of the fitted disc is represented by how dark the brown of the disc is in the plot. The NGTS 2021 disc model looks particularly different from the other three as its radius is greatly increased. This is likely due to the effects of stellar activity that were only observed during the model fit. These effects have likely lengthened the eclipse duration and so increased the radius of the disc model fit to the data.

Table 8. Results of MCMC fitting the tilted disc model to the phase curves for NGTS and *TESS*, along with the derived values from each of the model fits.

Value	NGTS (2017)	*TESS* S6	*TESS* S32	NGTS (2021)
y (d)	$-0.029^{+0.004}_{-0.001}$	$-0.032^{+0.006}_{-0.007}$	$-0.035^{+0.005}_{-0.016}$	$-0.040^{+0.006}_{-0.006}$
i (°)	$79.1^{+1.8}_{-1.3}$	$70.3^{+3.6}_{-5.1}$	67.9±5.1	$84.3^{+1.1}_{-1.8}$
ϕ (°)	$10.6^{+7.9}_{-2.4}$	$21.4^{+5.9}_{-8.6}$	$11.4^{+19.0}_{-9.6}$	$26.4^{+4.0}_{-2.4}$
r (d)	0.043±0.002	$0.045^{+0.009}_{-0.006}$	$0.031^{+0.023}_{-0.004}$	0.067±0.013
t_x	$0.450^{+0.054}_{-0.055}$	$0.515^{+0.053}_{-0.095}$	$0.165^{+0.172}_{-0.112}$	$0.265^{+0.144}_{-0.137}$
$hjd_{\rm central}$ (d)	$0.015^{+0.002}_{-0.001}$	$0.009^{+0.008}_{-0.006}$	$0.018^{+0.019}_{-0.002}$	0.033±0.011
r (au)	$(5.18 \pm 0.24) \times 10^{-3}$	$\left(5.42^{+1.08}_{-0.72}\right) \times 10^{-3}$	$\left(3.73^{+2.77}_{-0.48}\right) \times 10^{-3}$	$(8.07 \pm 1.56) \times 10^{-3}$
$M_{\rm min}$ ($M_{\rm J}$)	120 ± 19	142^{+88}_{-60}	40^{+89}_{-16}	1154 ± 694
χ^2	129.1	222.3	95.1	169.7
BIC	158.2	251.4	124.2	198.8

Downloaded from academic.oup.com/mnras/article/552/3/stag1802/8834030 by University of Sheffield user on 29 October 2026

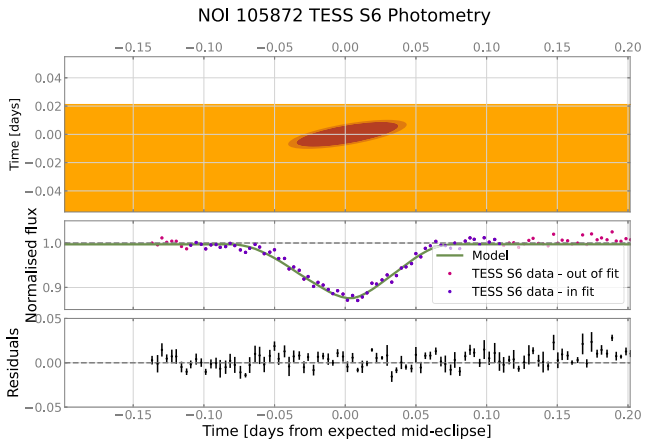


Figure 8. Tilted disc models for *TESS* Sector 6 modelled with original disc, but effects due to stellar activity (expansion of the disc) also modelled.

accompanying 'outer disc'. This represents the expansion of the disc as it is bombarded with radiation from stellar activity events, with the outer disc being more transparent than the original inner disc. This hypothesis also fits the data very well and could help to explain why the *TESS* eclipses are deeper than the NGTS eclipses, along with the possible disc precession.

If we take the NGTS 2017 fit then the radius of the disc is 5.18×10^{-3} au, and for this disc to be contained within the Hill sphere of the object then we calculated the object's minimum mass to be 120 M_J. If this is the case then the object is likely a small star and not a planet, but the only way to confirm this would be to get a constraint on the object's mass through spectroscopy. We also calculated the temperature of the disc using equation (8), which is generally used for calculating the equilibrium temperature of exoplanets.

$$T_{\rm eq} = T_* \cdot \sqrt{\frac{R_*}{f \cdot a}} \cdot (1 - A)^{\frac{1}{4}} \tag{8}$$

where T_* is the effective temperature of the host star, R_* is the radius of the host star, f is a multiplication factor based on the redistribution of heat across the surface, from day- to night-side, of the object, a is the semimajor axis and A is the albedo. The factor, f, we used is 2 because we assume uniform redistribution.

The temperature is found to be ≈ 1660 K. Using this we were able to calculate the likely depth of a secondary eclipse if the object is on a circular orbit, and this value came to 7.32 ± 0.13 per cent.

We wanted to check that the lack of a secondary eclipse is not due to the eccentricity and inclination of the orbit itself. By using the equations set out in A. Santerne et al. (2013) which satisfy the concepts from J. N. Winn (2010), we calculate the probability of seeing a secondary eclipse for this object. The lower limit probability of there being a primary eclipse but no secondary eclipse was calculated to be ~ 23 per cent, however it should be noted that the object radius used in this equation assumes that the object is spherical in shape, and the shape of a disc instead could change the value of this probability, although we do not think that this would be a major contributing factor. This calculation shows that it is possible that we see no secondary eclipse due to the orientation of the orbit; however, there could still be sinusoidal stellar activity effects as previously mentioned.

There are still a number of unanswered questions with this model. The model itself is relatively flexible, hence possibly why it fits our data so well, but we hope that with further observations, we could try and constrain our understanding of each model better and their plausibility. This is why we are focused on this hypothesis as our main one for now, but it cannot be confirmed or dirproven until we understand the system in its totality.

If we compare the chi-squared values for each data set across the eccentricity and tilted disc models, all of the data sets have a better fit with the tilted disc model. We made sure to keep the phase range and number of data points the same across each model fit for direct comparison. Because the models have a slightly different number of parameters we also compared the Bayesian Information Criterion (BIC) values for each model since this takes into account that a model with more parameters is more likely to be a better fit. The BIC values are also lower for the tilted disc model compared to the eccentricity model. This further compounds the tilted disc model as our most promising hypothesis so far.

5 CONCLUSIONS

We have presented a comprehensive photometric and spectroscopic investigation of the object NOI 105872, a young, short-period eclipsing system located in the Orion Nebula Cluster. Using multi-epoch photometry spanning nearly a decade from both ground-based and space-based facilities, we explored the origin of its unusually deep, asymmetric, and time-variable eclipse light curves.

The host star is confirmed to be a young (4.1 ± 0.4 Myr), discless pre-main-sequence M type star, based on spectroscopic indicators and spectral energy distribution modelling. The absence of infrared excess rules out a primordial circumstellar disc, placing constraints on scenarios involving large-scale dust structures associated with the star itself.

A range of hypotheses were examined to explain the observed eclipse morphology, including stellar activity, dipper-like behaviour, gravity darkening, orbital eccentricity, and atmospheric mass-loss from a disintegrating or evaporating planet. While some of these mechanisms may contribute second-order effects (particularly stellar activity), none are able to reproduce the depth, asymmetry, and long-term shape of the eclipse signal in a self-consistent manner.

Our modelling strongly favours a scenario in which the eclipsing structure is an extended, tilted circumsecondary disc surrounding a close-in companion. Parametric disc models fitted independently to multiple data sets consistently reproduce the observed eclipse profiles and yield a characteristic disc radius of ~ 0.005 au. While the inferred disc orientations vary modestly between epochs, these differences are consistent with slow disc precession and/or changes in disc structure driven by irradiation from the young, active host star. The presence of ingress features in some data sets is likely due to a combination of stellar activity and transient changes in disc opacity or vertical extent.

If the disc is gravitationally bound and confined within the Hill sphere of the companion, the inferred disc size implies a companion mass in the low-mass stellar regime. However, current spectroscopic data are insufficient to place meaningful constraints on the companion mass or radial velocity semi-amplitude. The absence of a detectable secondary eclipse can be explained by the system geometry and is not inconsistent with the proposed disc

Downloaded from academic.oup.com/mnras/article/552/3/stag1802/8834030 by University of Sheffield user on 29 October 2026

configuration. The lack of infrared excess can also be explained if we assume that the disc is too small to be seen in the IR data.

This enigmatic object therefore emerges as a candidate for a short-period circumsecondary disc system, but with the caveat that there must be follow-up observations to confirm its nature. Its proximity to the host star, youth, and apparent disc variability make it an important system for studying disc survival, evolution, and dynamics in extreme environments. Continued high-cadence, multi-wavelength photometric monitoring, along with higher signal-to-noise spectroscopic observations, will be crucial for confirming the nature of the companion, probing disc composition, and testing models of disc precession and irradiation-driven evolution.

There are only a handful of circumsecondary disc candidates, of which the shortest period one is orbiting every 5.4 d (T. J. David et al. 2016; K. Ohno et al. 2022). If confirmed, this system would provide a valuable benchmark for understanding circumsecondary discs and their role in shaping planetary and satellite systems around low-mass stars.

ACKNOWLEDGEMENTS

This work is based on data collected under the Next Generation Transit Survey (NGTS) project at the European Southern Observatory (ESO) La Silla Paranal Observatory. The NGTS facility is operated by a consortium institutes with support from the UK Science and Technology Facilities Council (STFC) under projects ST/M001962/1, ST/S002642/1, and ST/W003163/1. CAW and EdM would like to acknowledge support from the UK Science and Technology Facilities Council (STFC, grant number ST/X00094X/1). EG and MPB gratefully acknowledge support from UK Research and Innovation (UKRI) under the UK government's Horizon Europe funding guarantee for a European Research Council (ERC) starting grant [grant number EP/Z000890/1]. NM acknowledges support from the Department for the Economy (DfE) Northern Ireland postgraduate studentship scheme. This paper uses observations made at the South African Astronomical Observatory (SAAO). VSD and ULTRASPEC are supported by STFC grant ST/Z000033/1, a Leverhulme Research Fellowship (RF-2025-297/9) and the Spanish Ministry of Science, Innovation and Universities (PID2023-151588NB-I00).

The ULiege's contribution to SPECULOOS has received funding from the European Research Council under the European Union's Seventh Framework Programme (FP/2007-2013) (grant agreement no. 336480/SPECULOOS), from the Balzan Prize and Francqui Foundations, from the Belgian Scientific Research Foundation (F.R.S.-FNRS; grant n° T.0109.20), from the University of Liege, and from the Actions de Recherche Concertées (ARC) grant financed by the Wallonia–Brussels Federation. MG is F.R.S.-FNRS Research Director.

The Cambridge contribution is supported by a grant from the Simons Foundation (PI Queloz, grant number 327127).

JdW and MIT gratefully acknowledge financial support from the Heising–Simons Foundation, Dr and Mrs Colin Masson and Dr Peter A. Gilman for Artemis, the first telescope of the SPECULOOS network situated in Tenerife, Spain.

The Bern contribution to SPECULOOS is supported by the Swiss National Science Foundation (PP00P2-163967, PP00P2-190080 and the National Centre for Competence in Research PlanetS).

The Birmingham contribution to SPECULOOS has received fund from the European Research Council (ERC) under the European Union's Horizon 2020 research and innovation programme (grant agreement n° 803193/BEBOP), from the Mobilising European Research in Astrophysics and Cosmology (MERAC) foundation, and from the Science and Technology Facilities Council (STFC; grant n° ST/S00193X/1, ST/W002582/1, and ST/Y001710/1) and from the ERC/UKRI Frontier Research Guarantee programme (EP/Z000327/1/CandY).

DATA AVAILABILITY

The *TESS* data are accessible via the MAST (Mikulski Archive for Space Telescopes) portal at https://mast.stsci.edu/portal/ Mashup/Clients/Mast/Portal.html. Data from NASA/ATLAS are publicly available at https://fallingstar-data.com/forcedphot/. SPECULOOS-South data are available via the ESO archive portal at https://archive.eso.org/eso/eso_archive_main.html. Any code used for analysis or in producing the plots in this paper can be made available upon reasonable request to the author(s).

REFERENCES

Alencar S. H. P. et al., 2010, A&A, 519, A88
Almenara J. M. et al., 2022, A&A, 667, L11
Ansdell M. et al., 2016, ApJ, 816, 69
Baldwin J. A., Ferland G. J., Martin P. G., Corbin M. R., Cota S. A., Peterson B. M., Slettebak A., 1991, ApJ, 374, 580
Baraffe I., Homeier D., Allard F., Chabrier G., 2015, A&A, 577, A42
Barbary K., 2016, J. Open Source Softw., 1, 58
Barbieri M., 2023, preprint (arXiv:2312.06586)
Barnes J. W., 2007, PASP, 119, 986
Barnes J. W., 2009, ApJ, 705, 683
Barros S. C. C., Boué G., Gibson N. P., Pollacco D. L., Santerne A., Keenan F. P., Skillen I., Street R. A., 2013, MNRAS, 430, 3032
Bodenheimer P., 1965, ApJ, 142, 451
Bouma L. G., Jayaraman R., Rappaport S., Rebull L. M., Hillenbrand L. A., Winn J. N., David-Uraz A., Bakos G. Á., 2024, AJ, 167, 38
Bourrier V., Lecavelier des Etangs A., 2018, in Deeg H. J., Belmonte J. A. eds, Handbook of Exoplanets. Springer International Publishing AG, Cham, Switzerland, p. 148
Brogi M., Keller C. U., de Juan Ovelar M., Kenworthy M. A., de Kok R. J., Min M., Snellen I. A. G., 2012, A&A, 545, L5
Budaj J., 2013, A&A, 557, A72
Chiang E. I., Murray-Clay R. A., 2004, ApJ, 607, 913
Cody A. M., Hillenbrand L. A., 2018, AJ, 156, 71
Cody A. M. et al., 2014, AJ, 147, 82
Collier Cameron A., Robinson R. D., 1989, MNRAS, 238, 657
Coppejans R. et al., 2013, PASP, 125, 976
D'Orazi V., Randich S., Flaccomio E., Palla F., Sacco G. G., Pallavicini R., 2009, A&A, 501, 973
Da Rio N., Robberto M., Soderblom D. R., Panagia N., Hillenbrand L. A., Palla F., Stassun K., 2009, ApJS, 183, 261
Daley-Yates S., Jardine M. M., 2024, MNRAS, 534, 621
van Dam D. M. et al., 2020, AJ, 160, 285
David T. J. et al., 2016, Nature, 534, 658
David T. J. et al., 2017, ApJ, 835, 168
Delrez L. et al., 2018, in Marshall H. K., Spyromilio J., eds, Proc. SPIE Conf. Ser. Vol. 10700, Ground-based and Airborne Telescopes VII. SPIE, Bellingham, p. 21
Dhillon V. S. et al., 2014, MNRAS, 444, 4009
Dholakia S., Luger R., Dholakia S., 2022, ApJ, 925, 185
Donati J.-F., Landstreet J. D., 2009, ARA&A, 47, 333
Espinosa Lara F., Rieutord M., 2012, A&A, 547, A32
Fang M., van Boekel R., Wang W., Carmona A., Sicilia-Aguilar A., Henning T., 2009, A&A, 504, 461

Downloaded from academic.oup.com/mnras/article/552/3/stag1802/8834030 by University of Sheffield user on 29 October 2026

Farihi J., von Hippel T., Pringle J. E., 2017, MNRAS, 471, L145
Foreman-Mackey D., Hogg D. W., Lang D., Goodman J., 2013, PASP, 125, 306
Foster G., Poppenhaeger K., Ilic N., Schwope A., 2022, A&A, 661, A23
Gillen E. et al., 2020, MNRAS, 492, 1008
Gillon M., 2018, Nat. Astron., 2, 344
Grinin V., Stempels H. C., Gahm G. F., Sergeev S., Arkharov A., Barsunova O., Tambovtseva L., 2008, A&A, 489, 1233
Groote D., Hunger K., 1982, A&A, 116, 64
Günther M. N. et al., 2022, AJ, 163, 144
Hattori S., Foreman-Mackey D., Hogg D. W., Montet B. T., Angus R., Pritchard T. A., Curtis J. L., Schölkopf B., 2022, AJ, 163, 284
Hauschildt P. H., Allard F., Baron E., 1999, ApJ, 512, 377
Hayashi C., 1961, PASJ, 13, 450
Hillenbrand L. A., 1997, AJ, 113, 1733
Huang C. X. et al., 2020, Res. Notes Am. Astron. Soc., 4, 206
Ioannidis P., Huber K. F., Schmitt J. H. M. M., 2015, A&A, 585, A72
Jackman J. A. G. et al., 2020, MNRAS, 497, 809
Jardine M., Collier Cameron A., 2019, MNRAS, 482, 2853
Jeffries R. D. et al., 2017, MNRAS, 464, 1456
Jenkins J. M. et al., 2016, in Chiozzi G., Guzman J. C., eds, Proc. SPIE Conference Series Vol. 9913, Software and Cyberinfrastructure for Astronomy IV. SPIE, Bellingham, p. 99133E
Johns-Krull C. M., 2007, ApJ, 664, 975
Kearns K. E., Herbst W., 1998, AJ, 116, 261
Kenworthy M. A., Mamajek E. E., 2015a, Astrophysics Source Code Library, record ascl:1501.012
Kenworthy M. A., Mamajek E. E., 2015b, ApJ, 800, 126
Koen C., 2021, MNRAS, 500, 1366
Kounkel M., Covey K., 2019, AJ, 158, 122
Kreidberg L., 2015, PASP, 127, 1161
Lada C. J., Lada E. A., 2003, ARA&A, 41, 57
Lightkurve Collaboration, 2018, Astrophysics Source Code Library, record ascl:1812.013
Lovis C. et al., 2006, in McLean I. S., Iye M., eds, Proc. SPIE Conf. Ser. Vol. 6269, Ground-based and Airborne Instrumentation for Astronomy. SPIE, Bellingham, p. 62690P
Lucy L. B., 1967, ZAp, 65, 89
Luk'yanyk I., Kulyk I., Shubina O., Pavlenko Y., Vasylenko M., Dobrycheva D., Korsun P., 2024, A&A, 688, A65
Mamajek E. E., Quillen A. C., Pecaut M. J., Moolekamp F., Scott E. L., Kenworthy M. A., Collier Cameron A., Parley N. R., 2012, AJ, 143, 72
Mayor M. et al., 2003, The Messenger, 114, 20
McQuillan A., Mazeh T., Aigrain S., 2014, ApJS, 211, 24
Moulton T. et al., 2023, MNRAS, 521, 1700
Murray C. A. et al., 2020, MNRAS, 495, 2446
Ohno K., Thao P. C., Mann A. W., Fortney J. J., 2022, ApJ, 940, L30
Oshagh M., Santos N. C., Boisse I., Boué G., Montalto M., Dumusque X., Haghighipour N., 2013, A&A, 556, A19
Osterbrock D. E., Ferland G. J., 2006, Astrophysics of Gaseous Nebulae and Active Galactic Nuclei, 2nd. ed. University Science Books, Sausalito, CA
Portegies Zwart S. F., McMillan S. L. W., Gieles M., 2010, ARA&A, 48, 431
Pramono T. H., Kenworthy M. A., van Boekel R., 2024, A&A, 688, L11
Rebull L. M. et al., 2014, AJ, 148, 92
Ricker G. R. et al., 2015, J. Astron. Telesc. Instrum. Syst., 1, 014003
Rodríguez-Ledesma M. V., Mundt R., Pintado O., Boudreault S., Hessman F., Herbst W., 2013, A&A, 551, A44
Rodriguez J. E. et al., 2017, ApJ, 848, 97
Roggero N., Bouvier J., Rebull L. M., Cody A. M., 2021, A&A, 651, A44
Sanchis-Ojeda R., Winn J. N., Holman M. J., Carter J. A., Osip D. J., Fuentes C. I., 2011, ApJ, 733, 127
Sanchis-Ojeda R. et al., 2015, ApJ, 812, 112
Sanderson H., Jardine M., Collier Cameron A., Morin J., Donati J.-F., 2023, MNRAS, 518, 4734
Santerne A., Fressin F., Díaz R. F., Figueira P., Almenara J. M., Santos N. C., 2013, A&A, 557, A139
Savitzky A., Golay M. J. E., 1964, Anal. Chem., 36, 1627
Shingles L. et al., 2021, Release of the ATLAS Forced Photometry Server for Public Use, Transient Name Server AstroNote, 7, 1-7
Smith G. D. et al., 2021, MNRAS, 507, 5991
Smith G. D. et al., 2023, MNRAS, 523, 169
Smith J., Caldwell D., Jenkins J., Morris R., Rose M., Tenenbaum P., Ting E., Twicken J., 2020, American Astronomical Society Meeting Abstracts, 235, 174.02
Stauffer J. et al., 2015, AJ, 149, 130
Stauffer J. et al., 2017, AJ, 153, 152
Tonry J. L. et al., 2018, PASP, 130, 064505
Townsend R. H. D., Owocki S. P., Groote D., 2005, ApJ, 630, L81
Townsend R. H. D. et al., 2013, ApJ, 769, 33
Valio A., 2017, in Nandy D., Valio A., Petit P. eds, IAU Symposium Vol. 328, Living Around Active Stars. Cambridge Univ. Press, Cambridge, p. 69
Vines J. I., Jenkins J. S., 2022, MNRAS, 513, 2719
Watson C. A., Dhillon V. S., 2004, MNRAS, 351, 110
Waugh R. F. P., Jardine M. M., 2022, MNRAS, 514, 5465
Wheatley P. J. et al., 2018, MNRAS, 475, 4476
White R. J., Basri G., 2003, ApJ, 582, 1109
Winn J. N., 2010, in Seager S., ed., Exoplanets. University of Arizona Press, Tucson, AZ, p. 55
Winn J. N., Holman M. J., Johnson J. A., Stanek K. Z., Garnavich P. M., 2004, ApJ, 603, L45
von Zeipel H., 1924, MNRAS, 84, 665
Zhan Z. et al., 2019, ApJ, 876, 127
Zhu W. et al., 2022, ApJ, 933, L21

APPENDIX A: EXTRA FIGURES

Downloaded from academic.oup.com/mnras/article/552/3/stag1802/8834030 by University of Sheffield user on 29 October 2026

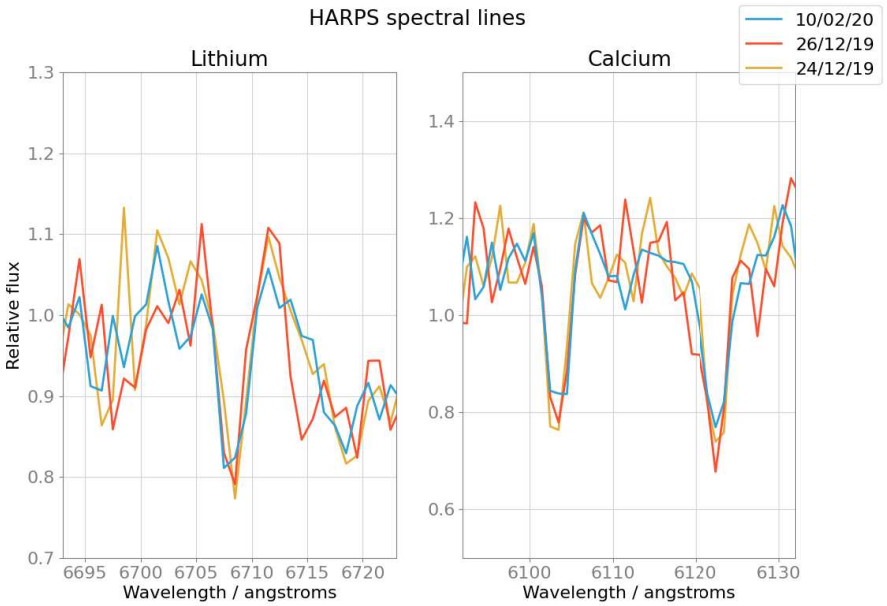


Figure A1. Lithum and Calcium absorption features in the three HARPS spectra. These observations have been sky-subtracted and binned into 1 Å chunks.

[1]*Astrophysics Research Centre, Queen's University Belfast, Northern Ireland, BT7 1NN, UK*
[2]*Astronomy Unit, Queen Mary University of London, Mile End Road, London E1 4NS, UK*
[3]*Leiden Observatory, Leiden University, Einsteinweg 55, NL-2333 CC Leiden, The Netherlands*
[4]*University Observatory, Faculty of Physics, Ludwig-Maximilians-Universität München, Scheinerstr. 1, D-81679 Munich, Germany*
[5]*Instituto de Astronomía, Universidad Católica del Norte, Angamos 0610, 1270709, Antofagasta, Chile*
[6]*Department of Physics, University of Warwick, Gibbet Hill Road, Coventry CV4 7AL, UK*
[7]*Centre for Exoplanets and Habitability, University of Warwick, Gibbet Hill Road, Coventry CV4 7AL, UK*
[8]*School of Physics and Astronomy, University of Leicester, University Road, Leicester LE1 7RH, UK*
[9]*Department of Physics and Astronomy, University of California Irvine, Irvine, CA 92697, USA*
[10]*Astrophysics Research Cluster, School of Mathematical and Physical Sciences, University of Sheffield, Sheffield S3 7RH, UK*
[11]*Instituto de Astrofísica de Canarias, E-38205 La Laguna, Tenerife, Spain*
[12]*LESIA, Observatoire de Paris, CNRS, Université Paris Diderot, Université Pierre et Marie Curie, F-92195 Meudon, France*
[13]*Université Paris-Saclay, Université Paris Cité, CEA, CNRS, AIM, F-91190 Gif-sur-Yvette, France*
[14]*Astrobiology Research Unit, Université de Liège, 19C Allée du 6 Août, 4000 Liège, Belgium*
[15]*Rugby School, Lawrence Sheriff St, Rugby, Warwickshire, CV22 5EH, UK*
[16]*Department of Earth, Atmospheric and Planetary Sciences, Massachusetts Institute of Technology, 77 Massachusetts Avenue, Cambridge, MA 02139, USA*
[17]*Instituto de Estudios Astrofísicos, Facultad de Ingeniería y Ciencias, Universidad Diego Portales, Av. Ejército Libertador 441, Santiago, Chile*
[18]*Centro de Excelencia en Astrofísica y Tecnologías Afines (CATA), Camino El Observatorio 1515, Las Condes, Santiago, Chile*
[19]*South African Astronomical Observatory, P.O. Box 9, Observatory, Cape Town 7935, South Africa*
[20]*Astrophysics Group, Keele University, Staffordshire, ST5 5BG, UK*
[21]*School of Physics & Astronomy, University of Birmingham, Edgbaston, Birmingham B15 2TT, UK*

This paper has been typeset from a TEX/LATEX file prepared by the author.

Downloaded from academic.oup.com/mnras/article/552/3/stag1802/8834030 by University of Sheffield user on 29 October 2026

© The Author(s) 2026.
Published by Oxford University Press on behalf of Royal Astronomical Society. This is an Open Access article distributed under the terms of the Creative Commons Attribution License (https://creativecommons.org/licenses/by/4.0/), which permits unrestricted reuse, distribution, and reproduction in any medium, provided the original work is properly cited.